in *Spectroscopy and Dynamics of Collective Excitations in Solids*
Ed. B. Di Bartolo (Plenum, NATO ASI series, 1996)

INTERACTION OF ULTRASHORT LASER PULSES WITH SOLIDS

Eric Mazur

Department of Physics
Harvard University
Cambridge, MA 02138

ABSTRACT

Beginning with some basic considerations in electromagnetic theory and solid state physics, I hope, in these four lectures, to develop some appreciation for the wonderfully rich electronic and optical properties of solids and to present an overview of current research in the area of the interaction of ultrashort laser pulses with solids.

The first two lectures are tutorials on the electronic and optical properties of solids and on energy transfer and relaxation in semiconductors. While some of the introductory material is treated in undergraduate courses, I will try to paint a broad picture and connect a number of facts that often remain disconnected. This introduction is followed by a survey of optical measurements of carrier and phonon dynamics in solids. I will conclude with an overview of recent experiments on electronic and structural changes induced by intense short laser pulses, including work done in my own research group.

I. ELECTRONIC AND OPTICAL PROPERTIES OF SOLIDS

In vacuum the frequency f and the wavelength λ of an electromagnetic wave are related by the speed c of light in vacuum,

$$f\lambda = c\,. \tag{1}$$

This yields a linear relation between the angular frequency $\omega \equiv 2\pi f$ and the wavevector $k \equiv 2\pi/\lambda$:

$$\omega = ck\,. \tag{2}$$

In a medium, the propagation of an electromagnetic wave is determined by the response of the material to electric and magnetic fields and is characterized by the

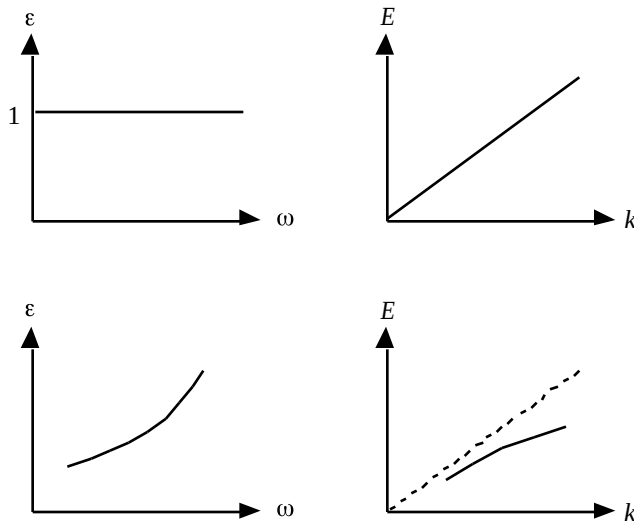

Figure 1. Dielectric function and energy-wavevector relationships in vacuum (top) and in a medium (bottom).

dielectric constant ε, the magnetic permeability μ, and the electric conductivity σ. Except for the magnetic permeability, which is nearly frequency independent at optical frequencies, the response of the medium depends on the frequency of the incident wave, and so dispersion occurs: waves of different frequencies propagate at different speeds. The frequency-dependent speed v of light in a medium is given by

$$v = \frac{c}{\mathrm{Re}\sqrt{\varepsilon(\omega)}} \equiv \frac{c}{n(\omega)}, \tag{3}$$

where $\varepsilon(\omega)$ is the frequency-dependent dielectric function and $n(\omega)$ the index of refraction of the medium. This frequency dependence results in a nonlinear relation between the angular frequency and the wavevector of the electromagnetic wave:

$$\omega = \frac{c}{\mathrm{Re}\sqrt{\varepsilon(\omega)}}\, k\,. \tag{4}$$

Figure 1 schematically shows the relationships between dielectric function and angular frequency, and between photon energy $E = \hbar\omega$ and wavevector, both in vacuum and in a medium. Throughout this part of my lectures I will use similar graphs to represent the optical properties of materials. The questions I will address are: why do different materials have different optical and electronic properties and what fundamental properties of solids are responsible for this behavior?

I. A. Propagation of Electromagnetic Waves through a Medium

The electromagnetic response of a material varies over the frequency spectrum because the charges present in the material respond at widely different frequencies. Roughly speaking, we can subdivide the charges into the following categories: ionic cores (the nuclei and core electrons at each lattice site), valence electrons, and free electrons. The ionic cores can form dipoles that tend to orient themselves along the direction of the applied external fields. This motion is usually limited to low

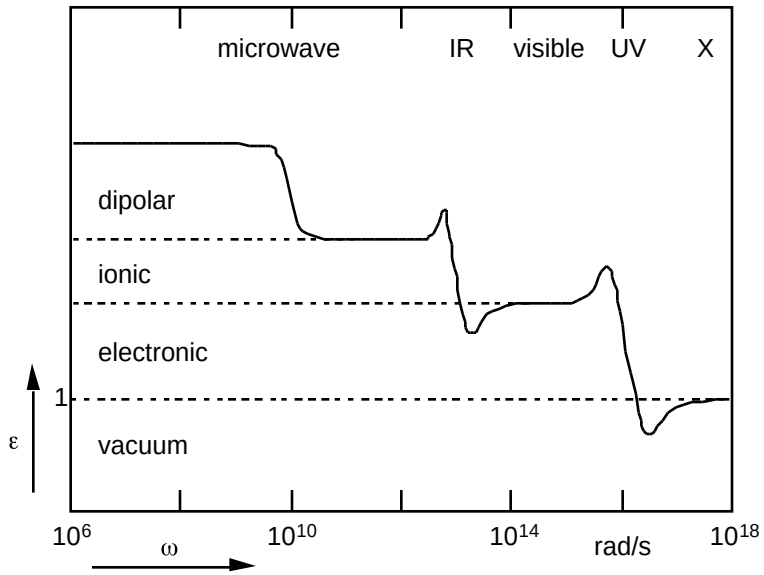

Figure 2. Schematic illustration of the various contributions to the dielectric constant across the electromagnetic spectrum.

frequencies and therefore only contributes to the polarization — and hence the propagation of the wave — at frequencies in the microwave region and below (see Fig. 2). At higher frequencies the dipoles can no longer follow the rapid oscillation of the applied field and their contribution to the dielectric constant vanishes. Lattice vibrations (displacement of the ionic cores) induced by the applied field contribute at frequencies up to the infrared region of the electromagnetic spectrum. In the visible and ultraviolet regions only the response of the free and bound valence electrons remain. Core electrons contribute at high frequency (10–1000 eV), but unless absorptions occur their contributions to the polarizability are generally small, and therefore the dielectric constant is close to 1 for x-rays. The dielectric function in Fig. 2 is very schematic — real materials generally show more structure and, depending on the type and number of charges present, some of the features shown may not be there.

Let us begin by analyzing the motion of a bound valence electron in response to an external driving field. If the field oscillates at frequency ω, the electron will oscillate at the same frequency with the phase and the amplitude of the oscillation determined by the binding and damping forces on the electron. The oscillation is described by the equation of motion of the electron [1]:

$$m\frac{d^2x}{dt^2} = -m\omega_o^2 x - m\gamma\frac{dx}{dt} - eE\,. \tag{5}$$

The first term on the right hand side of the equation represents a binding force with spring constant $k = m\omega_o^2$, where m and ω_o are the mass and the resonant frequency of the bound electron, respectively. The second term is a velocity-dependent damping force and the third term is the driving force with E the applied field. Rearranging terms and assuming a sinusoidally varying applied field of amplitude E_o and frequency ω, we obtain an inhomogeneous second-order differential equation

$$m\frac{d^2x}{dt^2} + m\gamma\frac{dx}{dt} + m\omega_o^2 x = -eE_o e^{-i\omega t}\,. \tag{6}$$

The steady-state solution of this equation, representing the oscillating motion of the electron, must be of the form

$$x(t) = x_o e^{-i\omega t}. \tag{7}$$

Substituting this into Eq. (6), we get for the amplitude of the motion

$$x_o = -\frac{e}{m}\frac{1}{(\omega_o^2 - \omega^2) - i\gamma\omega} E_o \ . \tag{8}$$

As is to be expected, the amplitude of the electrons is maximal when the driving frequency is equal to the resonance frequency. The motion of the electron results in an oscillating dipole moment

$$p(t) = -ex(t) = \left(\frac{e^2}{m}\right)\frac{1}{(\omega_o^2 - \omega^2) - i\gamma\omega} E_o e^{-i\omega t}. \tag{9}$$

In a sample with many bound electrons, the dipole moments of all the electrons contribute to a polarization

$$P(t) = \left(\frac{Ne^2}{m}\right)\sum_j \frac{f_j}{(\omega_j^2 - \omega^2) - i\gamma_j\omega} E(t), \tag{10}$$

where N is the total number of electrons, and f_j is the fraction of electrons having a resonant frequency ω_j and damping constant γ_j. In quantum mechanical terms, the factor Nf_j is the *oscillator strength*. This factor indicates how much each resonance contributes to the polarization.

The relation between the polarization P and the electric field E is usually written as $P(t) = \varepsilon_o \chi_e E(t)$, with χ_e the dielectric susceptibility. The dielectric constant is given by $\varepsilon(\omega) = 1 + \chi_e$, so that

$$\varepsilon(\omega) = 1 + \frac{Ne^2}{\varepsilon_o m}\sum_j \frac{f_j}{(\omega_j^2 - \omega^2) - i\gamma_j\omega} = \varepsilon'(\omega) + i\varepsilon''(\omega). \tag{11}$$

Figure 3 shows the frequency dependence of the dielectric constant for a single resonance and the resulting $E(k)$-behavior. At resonance, dissipation of energy is maximal since the amplitude of the electron motion is maximal. This dissipation of electromagnetic energy is what we call absorption and is reflected by the peak in the imaginary part of the dielectric constant at the resonance frequency. Note, also, that the real part crosses through zero near the resonance.

Let us next turn to the response of free electrons to an oscillating electromagnetic wave. Setting the binding force in Eq. (6) to zero we get

$$m\frac{d^2x}{dt^2} + m\gamma\frac{dx}{dt} = -eE_o e^{-i\omega t}. \tag{12}$$

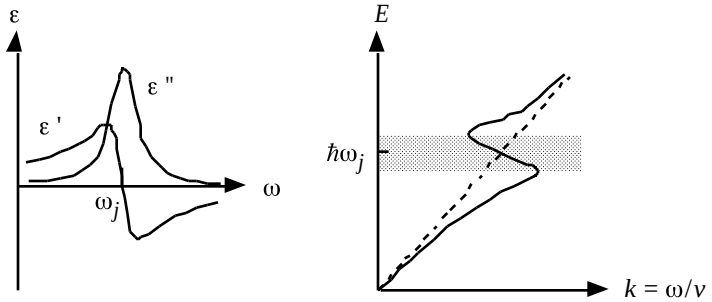

Figure 3. Frequency dependence of the dielectric constant near a resonance (left) and the resulting relation between energy and wavevector (right). The shaded region indicates the range of values for which absorption occurs.

Again, we obtain a solution of oscillating form,

$$x(t) = \frac{e}{m}\frac{1}{\omega^2 + i\gamma\omega}E_o e^{-i\omega t}, \tag{13}$$

but because there is no binding term, the motion does not exhibit any resonances. At low frequency, $\omega/\gamma << 1$, the applied electric field induces a time-varying current

$$J(t) \equiv \frac{dq}{dt} = -Ne\frac{dx}{dt} = \frac{Ne^2}{m}\frac{1}{\gamma - i\omega}E(t) \approx \frac{Ne^2}{m\gamma}E(t) \equiv \sigma E(t), \tag{14}$$

where N is the number of free electrons and σ the conductivity.

At high frequency the current can no longer keep up with the driving field and we may no longer ignore the imaginary part of the conductivity. Let us therefore again consider the oscillating dipole moment created by each electron:

$$p(t) = -ex(t) = -\left(\frac{e^2}{m}\right)\frac{1}{\omega^2 + i\gamma\omega}E_o e^{-i\omega t}. \tag{15}$$

For a sample with N free electrons, this gives a polarization

$$P(t) = -\left(\frac{Ne^2}{m}\right)\frac{1}{\omega^2 + i\gamma\omega}E(t) \equiv \varepsilon_o\chi_e E(t). \tag{16}$$

From this expression we obtain the free-electron contribution to the dielectric constant:

$$\varepsilon(\omega) = 1 - \left(\frac{Ne^2}{m\varepsilon_o}\right)\frac{1}{\omega^2 + i\gamma\omega} = \varepsilon'(\omega) + i\varepsilon''(\omega). \tag{17}$$

If the damping is negligible, $\gamma << \omega$, the imaginary part of the free-electron contribution vanishes and the real part becomes

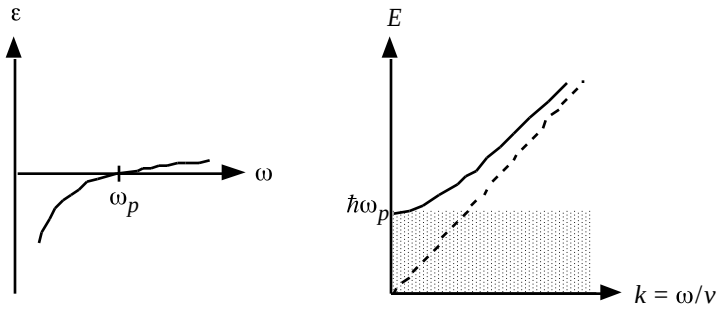

Figure 4. Dielectric function and $E(k)$ behavior for a plasma of free electrons with zero damping. The shaded region corresponds to a forbidden band of frequencies. Electromagnetic waves within this region are strongly attenuated.

$$\varepsilon'(\omega) = 1 - \frac{Ne^2}{m\varepsilon_o}\frac{1}{\omega^2} \equiv 1 - \frac{\omega_p^2}{\omega^2}, \tag{18}$$

where ω_p is called the plasma frequency. For frequencies below the plasma frequency, the dielectric constant is negative and so the index of refraction is purely imaginary resulting in strong attenuation of the electromagnetic wave (see Fig. 4). In the $E(k)$-plot this attenuation gives rise to a range of 'forbidden frequencies', or frequency gap below the plasma frequency. In this regime, however, the reflectivity is nearly one and incident electromagnetic waves do not penetrate into the plasma. Above the frequency gap the electromagnetic wave propagates through the medium and at high frequency the dielectric function approaches unity. The free electrons thus act like a high-pass filter: below the plasma frequency reflection occurs; above the plasma frequency the free electrons are transparent. For intrinsic semiconductors, the plasma frequency lies in the microwave or infrared part of the electromagnetic spectrum.

The effect of small, but nonzero damping is illustrated in Fig. 5. The damping results in a nonzero imaginary part at low frequency and a reduction of the frequency gap in the $E(k)$-plot. At high frequency the real part still approaches unity and the imaginary part vanishes.

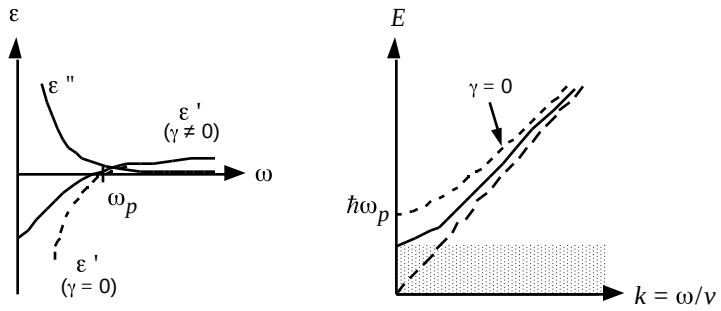

Figure 5. Dielectric function and $E(k)$ behavior for a plasma of free electrons with small nonzero damping. The effect of the damping is to reduce the forbidden band of frequencies.

Type	*Attractive Interaction*	E_{coh} (eV)	a (nm)
covalent	overlap of charge distribution	3–10	0.2
ionic	electrostatic	6-9	0.2–0.3
metallic	delocalized overlap of charge distribution	1–5	0.3–0.4
van der Waals	induced dipole-dipole	0.01–0.1	0.4
Hydrogen	electrostatic	0.3–1	0.4

Table 1. Bond types with typical bond energies E_{coh} and bond lengths a.

I. B. Chemical Bonds and Electronic Bands

The simple model given above describes the dielectric behavior for bound and free electrons. To what extent there are free or bound charges in a material strongly depends on the nature of the chemical bonds between the atoms in the material [2]. These bonds are due to an interplay between attractive and repulsive interactions between the atoms — the attraction makes it possible for atoms in a solid to have lower total energy than the same atoms when they are well separated, while the repulsion prevents the solid from collapsing onto itself. Table 1 provides an overview of the different types of bonds that can occur between atoms in a solid. The differences between these bonds are mainly due to differences in the mechanism responsible for attraction. The repulsive mechanisms are due to a combination of an electrostatic repulsion of the ionic cores, a repulsion due to the confinement of valence electrons, and a repulsion due to the Pauli exclusion principle.

The strongest bond is the covalent bond which is formed by an overlap of charge distribution between neighboring atoms. The lowering of the total energy comes about because the sharing of electrons makes it possible to fill bands. Figure 6*a* schematically illustrates covalent bonding between two atoms. If the two atoms get close enough for the atomic orbitals to overlap, then the wavefunctions of these orbitals can add with either the same or opposite phase. This results in a splitting of the energy level of the overlapping orbitals. The lower level corresponds to the wavefunctions adding in phase while the upper level corresponds to adding with opposite phase. If both of the original electronic levels in each atom were singly occupied, then in the ground state of the new system, the two electrons will occupy the lower level, which is lower in energy than the original level. Since this state is energetically more favorable than the state in which the two atoms are separated, the sharing of the two electrons results in a bond between the two atoms. If one or both of the electrons is excited to the upper level, then the new state no longer has

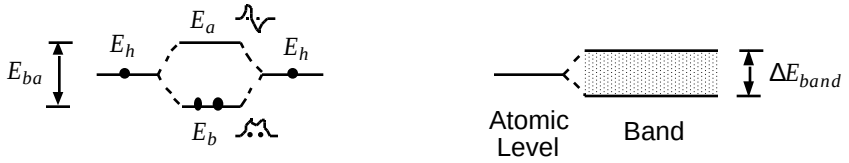

Figure 6. Energy level splitting in a covalent bond between two atoms (left) and energy-level broadening into a band in a covalently bonded solid (right).

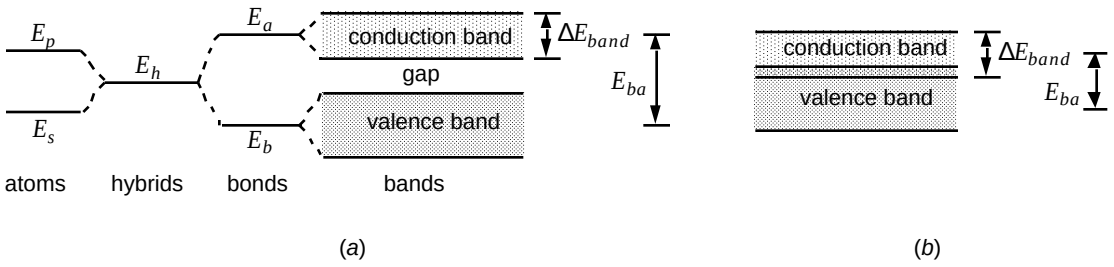

(*a*) (*b*)

Figure 7. Broadening of bonding and anti-bonding levels into valence and conduction bands. In insulators and semiconductors the bonding-antibonding splitting E_{ba} is larger than the width of the bands so the valence band is completely filled and the conduction band completely empty (left). In metals the two bands overlap resulting in a partially filled band (right).

a lower total energy than the state with two separated atoms. Thus, the lower level corresponds to a bonding state while the upper level corresponds to an antibonding state. In the case of a solid consisting of many atoms, the bonding and antibonding levels broaden into bands (see also Figs. 6*b* and 7*a*).

Covalently bonded solids are made up either of nonmetallic elements or a combination of a metallic and a nonmetallic element. The sharing of electrons between neighboring atoms results in strongly directed bonds, and as a consequence covalently bonded solids tend to be stiff and brittle. Moreover, due to the strong localization of the valence electrons covalent solids have zero or low conductivity.

Ionic bonds form when two neighboring atoms can fill their outer shell by exchanging one or more electrons. This results in a strong electrostatic attraction and a lower energy state. Ionic solids are always made up of a combination of metallic and nonmetallic elements, and the strong localization of the valence electrons results in a vanishingly small conductivity. Depending on the extent to which charge is transferred from one atom to another (as opposed to being shared), bonds can exhibit a broad spectrum of behavior between that of an ionic or covalent solid.

Metallic bonding arises from a more delocalized overlap of atomic orbitals in a solid. This type of bonding can only occur for a relatively large number of atoms and the delocalized nature of the bond results in materials that can be deformed and that are softer than covalent or ionic solids. The overlap of the orbitals of a particular atomic energy level leads to a broadening of this energy level into a band of energies. If the atomic energy levels are not fully occupied, then the total energy is lower for the atoms in a solid than for isolated atoms, as illustrated schematically in Fig. 7*b*. The partial occupation of the atomic levels results in a partially-filled energy band, and so the material exhibits metallic electronic characteristics [3].

Table 1 lists two more bonding mechanisms: the van der Waals bond and the hydrogen bond, both of which are extremely weak. The van der Waals bond is due to an induced dipole-dipole interaction. Hydrogen bonds are formed when covalently bonded hydrogen atoms in one molecule attract an atom in another molecule due to a dipole interaction (pointing toward the hydrogen atom).

In these lectures we will mainly be concerned with semiconductors which exhibit characteristics of both covalent ionic bonding and metallic bonding. On the one hand, nearest neighbors form covalent bonds by sharing two electrons, resulting in a splitting of atomic levels into bonding and antibonding states. On the other hand, these bonding and antibonding states are broadened into bonding and antibonding energy bands by more delocalized interactions with the other atoms in the solid. When the average bonding-antibonding splitting in the material is larger than the width of the energy bands, an energy gap will exist between the bonding

and the antibonding bands (see Fig. 7a). If the atomic orbitals start out half-filled, then the ground state consists of a fully occupied bonding band and an empty antibonding band. In this case the material will not conduct electricity. However, when the average bonding-antibonding splitting is smaller than the width of the energy bands, the bonding and antibonding bands overlap (see Fig. 7b). The resulting partially-filled bands lead to metallic electronic characteristics even in the ground state. A semiconductor corresponds to the former case: an energy band gap separates the bonding (valence) and antibonding (conduction) bands. While semiconductors are insulators in the ground state, they start conducting when electrons are excited from the valence to the conduction band. Conductivity in a semiconductor is mediated both by the negatively charged electrons excited to the conduction band and by the positive holes left behind in the valence band by the excited electrons. The conducting electrons and holes are often referred to collectively as free charge carriers, or simply free carriers.

The existence of electronic energy levels and energy bands is inherently quantum mechanical. To determine the energy levels for a certain system one must know the potential energy function $U(\mathbf{r})$ for the electrons in the system and solve the Schrödinger equation

$$\nabla^2\psi + \frac{2m}{\hbar^2}\left[E - U(\mathbf{r})\right]\psi = 0\,. \tag{19}$$

Here, ψ is the wavefunction of the electron, m its mass and E its energy. By substituting a certain potential energy function $U(\mathbf{r})$ and assuming a certain form for the wavefunction ψ, one can solve for the allowed energies E. Analytic solutions to the Schrödinger equation exist only for a few limited cases. Without providing any derivations, we will briefly review these cases because even though they do not correspond to any realistic situations, they do provide insight as to what gives rise to the electronic bandstructure of solids.

The simplest situation one can consider is that of a free particle. In that case the potential function is zero, $U(\mathbf{r}) = 0$, and the solution to the Schrödinger equation yields the standard parabolic relation between kinetic energy and momentum [4]:

$$E = \frac{\langle p\rangle^2}{2m}\,. \tag{20}$$

The energy of the free particle can take on any positive value, and hence the energy spectrum of the particle is a semi-infinite band (see Fig. 8*a*).

The energy of a particle confined to a one-dimensional infinite potential well,

$$\begin{aligned} U(x) &= 0 \quad (0 < x < a) \\ U(x) &= \infty \quad (x \le 0,\, x \ge a) \end{aligned} \tag{21}$$

can only take on discrete values [4],

$$E_n = \frac{n^2\pi^2\hbar^2}{2ma^2}\,, \tag{22}$$

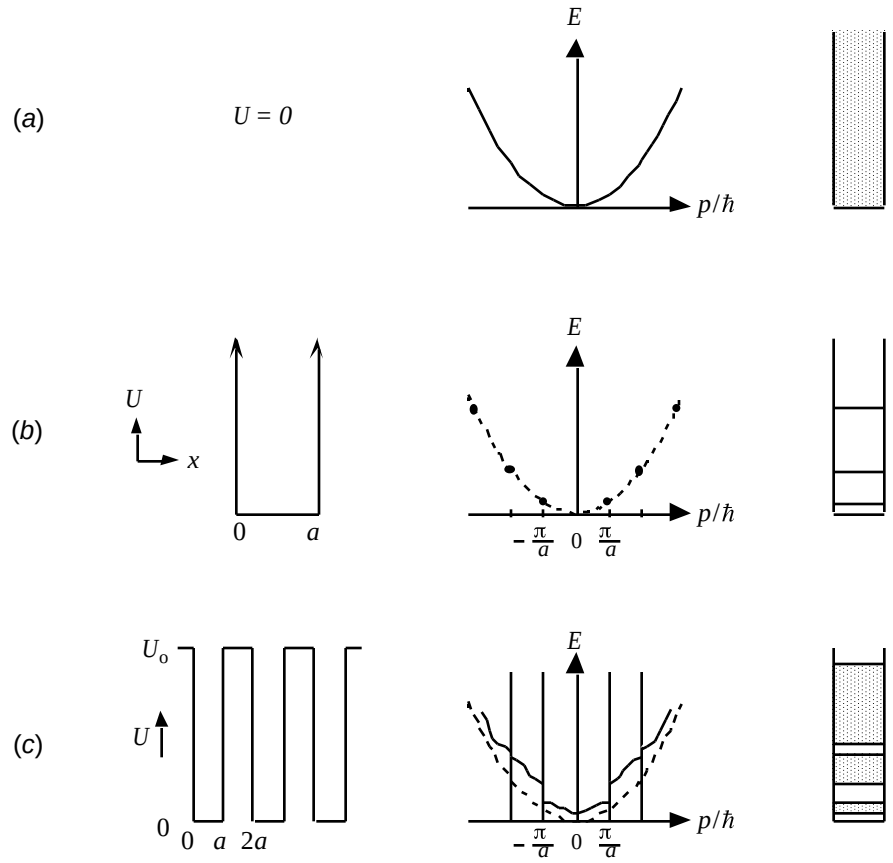

Figure 8. Solutions to the Schrödinger equation for three different potential energy functions: (*a*) free particle, (*b*) infinite square well, (*c*) periodic square well (Kronig-Penny model). The graphs on the right show the allowed values of energy.

where n is a positive integer. The energy spectrum exhibits a single level for each value of n (see Fig. 8*b*).

A solid can be idealized as a periodic potential of finite potential wells (see Fig. 8*c*). For this simplified situation the Schrödinger equation can still be solved analytically by substituting periodic Bloch functions [5]

$$\psi(\mathbf{k}, \mathbf{r}) = e^{i\mathbf{k}\cdot\mathbf{r}} u(\mathbf{k}, \mathbf{r}), \tag{23}$$

where $\mathbf{k}$ is a constant vector and $u(\mathbf{r})$ is a function with the same periodicity as the lattice, *i.e.*, $u(\mathbf{k},\mathbf{r}+\mathbf{R}) = u(\mathbf{k},\mathbf{r})$ for any lattice vector $\mathbf{R}$. The resulting allowed values of energy are schematically illustrated in Fig. 8*c*. The periodic potential introduces a perturbation which segments and distorts the free-particle solution (Fig. 8*a*). Instead of the discrete values of energy found for a particle in a single, infinite well, we now find that the energy of a particle can take on values in a number of separate energy bands.

For a real solid the potential along a line of atoms is schematically illustrated in Fig. 9. Inside the solid the potential is periodic and has the same value at any two points separated by a lattice vector, except near the edge of the solid where the potential energy rises to zero. Near each nucleus the potential energy forms a deep well, closely approaching that of an isolated atom. In the region between the atoms, many atoms contribute to the potential energy and hence the total energy is lower than outside the solid.

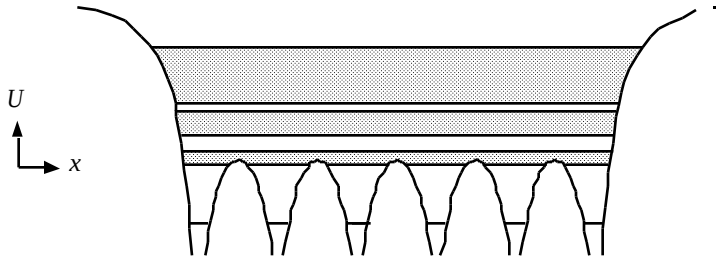

Figure 9. Electron potential energy along a line of atoms in a solid. The shaded regions indicate the allowed energy bands for the electrons.

The core electrons have energies that are deep in the potential energy wells near the atomic nuclei and the wavefunctions for these core electrons are nearly identical to those in an isolated atom. At higher energies, the wavefunctions extend throughout the solid and the allowed energy levels spread into bands. Whether or not a solid is conductive depends on the position of the Fermi level with respect to the bands. Since each level in an atom has two allowed states, N atoms contribute $2N$ states to each band. Therefore, if the number of electrons per unit cell is odd, the highest band is only half filled and the solid is a conductor. In the case of an even number of electrons per unit cell, the solid can still be a conductor if the bands overlap. If they don't the solid is an insulator or semiconductor. An example is shown in Fig. 10.

Figure 11 schematically illustrates the absorption coefficient of a typical semiconductor. The sharp rise in absorption in the visible region is the fundamental absorption edge: electrons are excited from the highest occupied band to a higher, unoccupied band. Below this absorption edge, ionic or partially ionic solids can absorb infrared radiation at specific resonances and the photon energy is converted to phonons (lattice vibrations). In addition, free carriers (electrons in the conduction band or holes in the valence band) can absorb radiation. Due to the very low density of free carriers in semiconductors, however, this contribution is small and limited to the microwave part of the electromagnetic spectrum. For metals, the free-carrier contribution is larger and shifts to higher frequency, while the fundamental absorption edge is absent. Conversely, for insulators, free-carrier absorption is absent and the fundamental absorption shifts toward higher frequency.

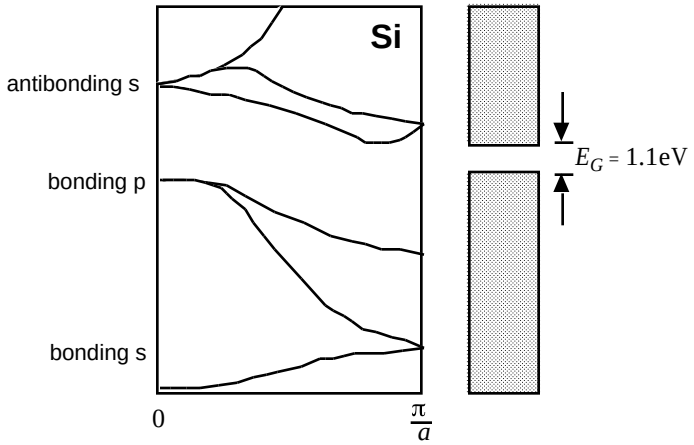

Figure 10. Bandstructure for silicon (left) and corresponding allowed energy bands (right). After Ref. [6].

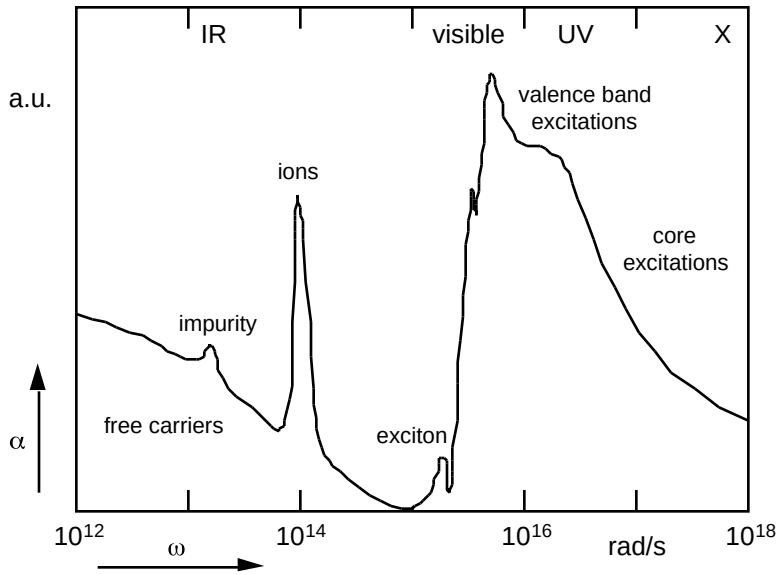

Figure 11. Absorption coefficient for a hypothetical semiconductor.

I. C. Phonons

In the previous two sections I assumed the ionic lattice to be fixed and immobile. In this section I consider collective motions of the ions. The ions can be displaced from their equilibrium positions and such disturbances can travel through the solid in the form of phonons which play an important role in the electronic and optical properties of solids because they can interact directly with electromagnetic waves.

Let us begin by considering a linear chain of identical atoms separated by a spacing *a* as illustrated in Fig. 12. The top of the drawing shows the atoms in their equilibrium position; at the bottom the atoms are displaced from their equilibrium position. Let us furthermore assume that only nearest neighbors exert forces on each other and that the interionic force obeys Hooke's law. The forces exerted on ion *n* by its two nearest neighbors are thus

$$\begin{aligned} F_{n-1,n} &= \gamma\,(u_{n-1} - u_n) \\ F_{n+1,n} &= \gamma\,(u_{n+1} - u_n) \end{aligned} \tag{24}$$

where γ is the force constant. The equation of motion for the ion is then

$$m\,\frac{d^2u_n}{dt^2} = \gamma\left[u_{n-1} + u_{n+1} - 2u_n\right]. \tag{25}$$

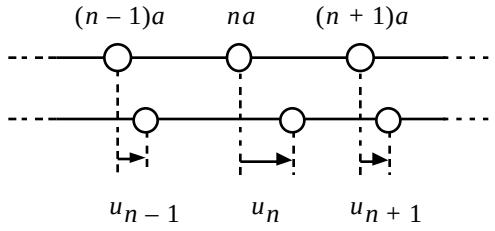

Figure 12. Vibrating linear chain of identical atoms spaced by a distance *a*.

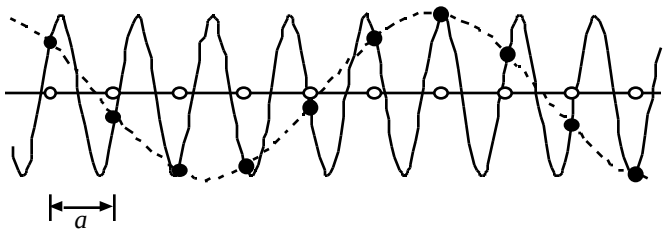

Figure 13. Oscillating chain of atoms showing instantaneous displacements. The solid curve conveys no information not given by the dashed one.

We look for solutions in the form of a traveling harmonic displacement wave (called a normal mode)

$$u_n(t) = Ae^{i(qna-\omega t)}, \tag{26}$$

where A is the amplitude of the displacement wave, q the wavevector, and ω the angular frequency. Substituting this into Eq. (25) we get

$$-m\omega^2 = \gamma\,[e^{-iqa} + e^{iqa} - 2] = -4\gamma \sin^2\!\left(\frac{qa}{2}\right), \tag{27}$$

so

$$\omega = \sqrt{\frac{4\gamma}{m}}\left|\sin\frac{qa}{2}\right|. \tag{28}$$

As Fig. 13 shows, we only need to consider displacement waves of wavelength larger than $2a$ — due to the discreteness of the chain, all waves of shorter wavelengths are equivalent to certain waves of longer wavelengths. This means we can restrict our analysis to small wavevectors:

$$\lambda \geq 2a \qquad q \leq \frac{\pi}{a} \tag{29}$$

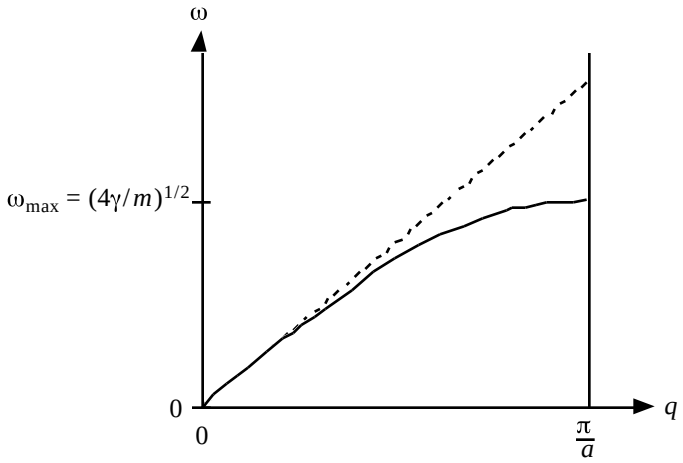

Figure 14. Dispersion of waves along a linear chain of atoms. The dashed line shows the result one would obtain for a continuous medium. The slope of the dashed line corresponds to the speed of sound waves in the medium.

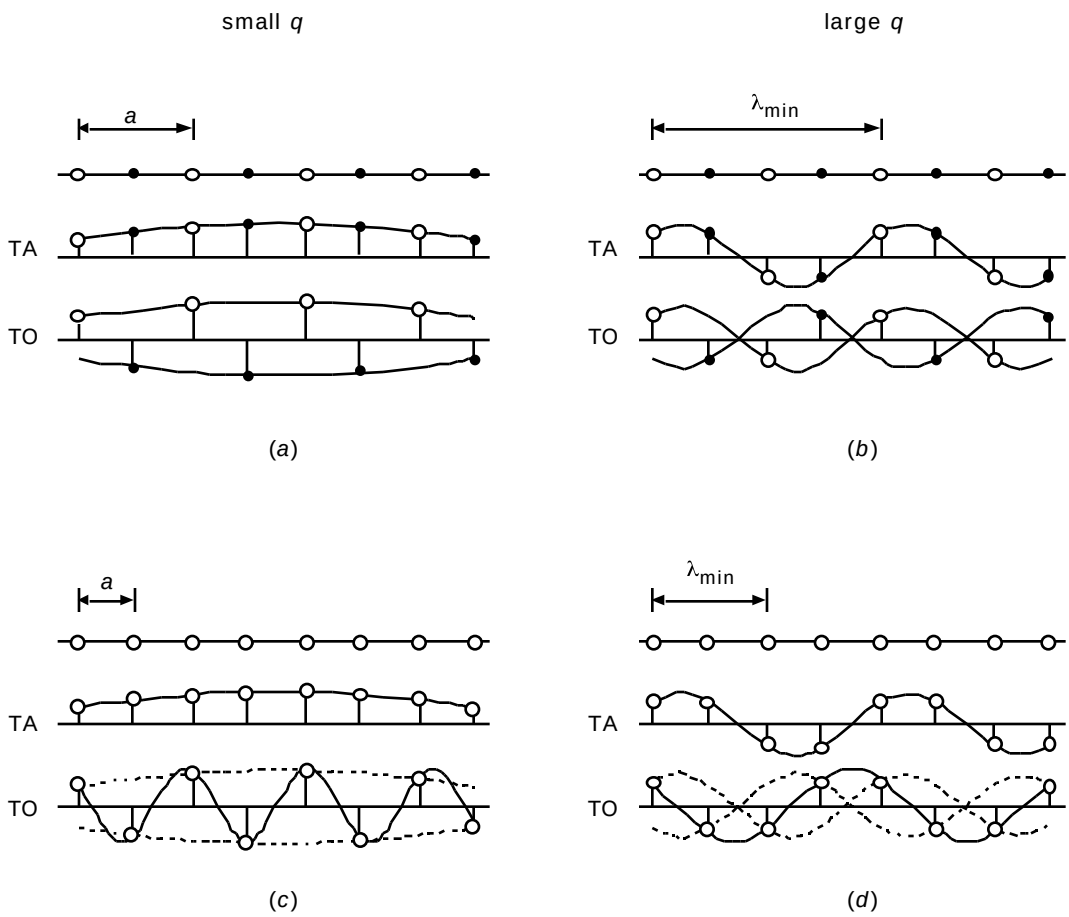

Figure 15. Waves on two-atom linear chains. Displacements are shown for (*a*) small and (*b*) large wavevector. The in- and out-of-phase waves correspond to acoustic and optic phonons, respectively. The bottom to graphs (*c* and *d*) show how the waves for a two-atom chain map onto waves of different wavevector for a one-atom chain.

Figure 14 shows the dependence of the displacement frequency on wavevector q (Eq. 28). For small wavevector, Eq. (28) becomes linear in the wavevector

$$\omega = \sqrt{\frac{4\gamma}{m}}\,\frac{qa}{2} = \sqrt{\frac{\gamma\, a}{m\,/\,a}}\,q = v_s q\,, \tag{30}$$

with v_s the speed of sound. This is the relation one would obtain if the chain were continuous rather than discreet (when a approaches zero, π/a goes to infinity and the dispersion relation becomes linear throughout). The dispersion of waves near the edge of the Brillouin zone at π/a is therefore a direct consequence of the granularity of the chain.

In a two-atom linear chain the situation is more complicated because the atoms of different kind can either move in phase (such displacement waves are called acoustic phonons) or out of phase (optic phonons). Figure 15*a* illustrates the displacements that occur for transverse acoustic and optic phonons of small wavevector. While both displacements have the same large wavelength, the potential energy associated with the optic phonon is larger because the interatomic bonds are much more distorted. The dispersion relation now has two branches (see Fig. 16*a*); for low wavevector the acoustic branch approaches zero, but because of the large distortion at low frequency, the corresponding energy for the optic branch is nonzero at zero wavevector.

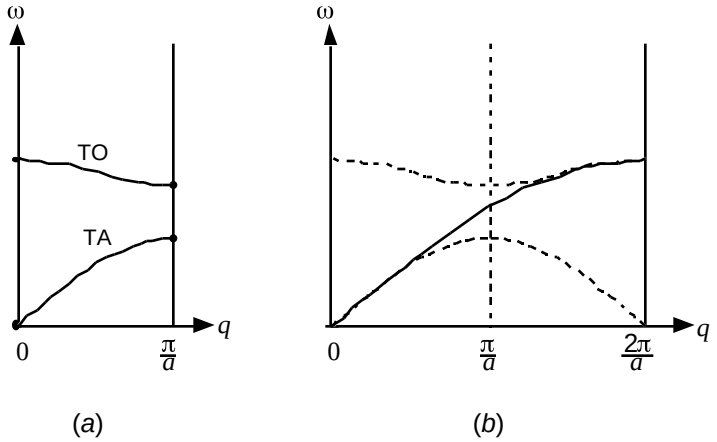

Figure 16. Dispersion relation for phonons (*a*) on a two-atom linear chain and (*b*) on a corresponding one-atom linear chain..

Figure 15*b* shows the displacements for the acoustic and optic phonons of the shortest possible wavelength (2*a*). The corresponding energies (see Fig. 16*a*) are slightly different. Figures 15*c* and 15*d* show how the cases illustrated in Figs. 15a and 15*b* relate to single-atom chain phonons: the optic branch vanishes as low wavevector optic phonons map onto large wavevector acoustic phonons. Note, in particular that the low-*q* TO phonon for the two-atom chain maps to a hiqh-*q* TA phonon on the one-atom chain (*cf.* Figs. 15*a* and *c*). Similarly, the TO and TA phonon modes at the edge of the Brillouin zone for the two-atom chain, are identical on the one-atom chain (*cf.* Figs. 15*b* and *d*), but are now in the middle of a Brillouin zone that is twice as wide (Fig. 16*b*).

I. D. Nonlinear Optical Interactions

In this section we consider the nonlinear optical properties of materials. In the presence of an electric field $E(t)$, atoms in a solid become polarized giving rise to a polarization of the solid. For small electric fields, the induced polarization is linear in the applied field:

$$P(t) = \chi^{(1)} E(t)\,, \tag{31}$$

with $\chi^{(1)}$ the linear susceptibility. For large applied fields, however, the induced polarization becomes nonlinear in the applied field [7, 8]:

$$\begin{aligned} P(t) &= \chi^{(1)} E(t) + \chi^{(2)} E^2(t) + \chi^{(3)} E^3(t) + \quad = \\ &= P^{(1)}(t) + P^{(2)}(t) + P^{(3)}(t) + \end{aligned} \tag{32}$$

The first term represents the linear polarization, $P^{(n)}$ the n-th order polarization, and $\chi^{(n)}$ the n-th order nonlinear optical susceptibility. In general, the n-th order nonlinear susceptibility is not a scalar, but a tensor of rank $(n+1)$. For typical materials the electric field has to be of the order of atomic field strengths E_{at} before the second-order term becomes comparable to the linear term:

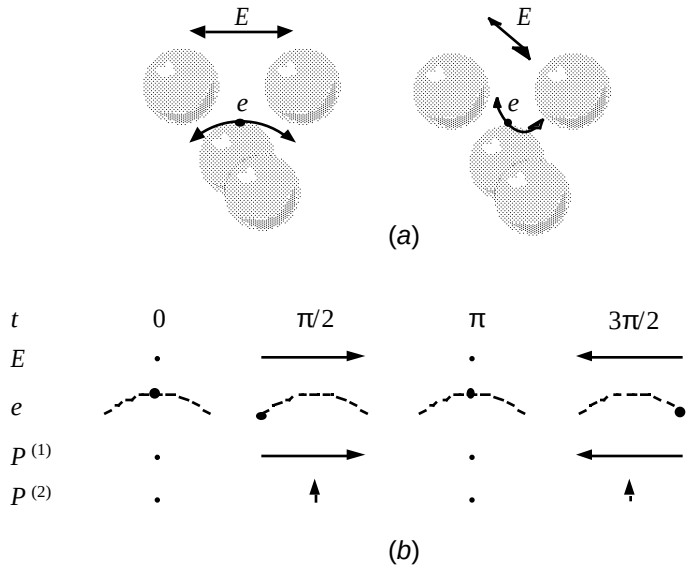

Figure 17. (*a*) An electron in the interstitial region between four atoms oscillates along a curved equipotential plane. (*b*) This oscillation causes a small second-order dipole in a direction perpendicular to the first-order dipole. The period of oscillation of the second-order dipole is one-half that of the first-order one.

$$\chi^{(n)} \approx \frac{\chi^{(1)}}{E_{at}^{n-1}}. \tag{33}$$

The nonlinear polarization can drive a new field. According to the wave equation that follows from the Maxwell equations, we have [1]

$$^2E - \frac{n^2}{c^2}\frac{\partial^2 E}{\partial t^2} = \frac{4\pi}{c^2}\frac{\partial^2 P^{NL}}{\partial t^2}. \tag{34}$$

The second-order polarization, for instance, causes a driving term proportional to the square of the applied electric field, resulting in a new field at twice the applied frequency.

Consider an electron in the interstitial region between four atoms, as shown in Fig. 17*a*. Physically, the doubling of the frequency comes about because the charges move along a curved potential plane. For an electric field oscillating in the plane of the drawing, the electron moves along the dotted arc; in addition to being displaced in the horizontal direction, the electron also undergoes a small vertical displacement. This vertical displacement gives rise to a small second-order dipole moment perpendicular to the horizontal first-order dipole moment. As Fig. 17*b* shows, the period of oscillation of the second-order dipole moment is half that of the first-order dipole moment.

For systems with inversion symmetry, however, the second-order susceptibility vanishes. This can readily be seen by writing the second term of Eq. (32) in tensorial form:

$$\mathbf{P}^{(2)} = \chi^{(2)} : \mathbf{EE}. \tag{35}$$

Applying inversion, we get

$$-\mathbf{P}^{(2)} = \chi^{(2)} : (-\mathbf{E})(-\mathbf{E}), \tag{36}$$

and from Eqs. (35) and (36) we see that $\chi^{(2)} = -\chi^{(2)}$, which can only be satisfied if $\chi^{(2)}$ vanishes.

For systems that do not have inversion symmetry $\chi^{(2)}$ is not zero and an intense field will cause a second-order polarization. Let the applied field be of the form

$$E(t) = \tfrac{1}{2} E e^{i\omega t} + \text{c.c.} \tag{37}$$

The second-order polarization is then

$$P^{(2)} = \chi^{(2)} E^2(t) = \tfrac{1}{2}\chi^{(2)} EE^* + \tfrac{1}{4}\left\{\chi^{(2)} E^2 e^{-i2\omega t} + \text{c.c}\right\}. \tag{38}$$

The second term on the right-hand side oscillates at frequency 2ω and can drive a new electromagnetic wave at double the incident frequency. This process is called second-harmonic generation.

If two oscillating fields of different frequency are present,

$$E(t) = \tfrac{1}{2} E_1 e^{i\omega_1 t} + \tfrac{1}{2} E_2 e^{i\omega_2 t} + \text{c.c.}, \tag{39}$$

the second-order polarization contains terms at frequencies $2\omega_1$, $2\omega_2$, at the sum-frequency $\omega_1+\omega_2$, at the difference frequency $\omega_1-\omega_2$, and at zero frequency. Because of dispersion the output beam at these new frequencies and the input beams at ω_1 and ω_2 travel at different velocities. To maximize output at any of the new frequencies it is therefore necessary to geometrically match the phases of the input and output beams [8].

Let us next briefly turn to the third-order polarization which 'mixes' four electric fields — three input fields generate one new output field. When three different input frequencies are present, 13 new frequencies can be generated. An example of a third-order effect is coherent anti-Stokes Raman spectroscopy (CARS). Two of the input frequencies are chosen such that their difference matches a resonant frequency in the system: $\omega_1 - \omega_2 = \omega_{res}$. The beating between the two input beams then coherently populates the upper level of the resonance. A third beam at frequency ω_3 then beats with the resonant oscillation in the system, generating a fourth beam at the anti-Stokes Raman frequency $\omega_a = \omega_1 - \omega_2 + \omega_3$. Note that this process is parametric, *i.e.*, the initial and final state is the same. The intensity of the coherent anti-Stokes beam is proportional to the population difference between the lower and upper levels of the resonance [8]. Hence, CARS can be used to measure population distributions.

II. ENERGY TRANSFER AND RELAXATION IN SEMICONDUCTORS

Next we turn our attention to the interaction between carriers, phonons, and photons in semiconductors and to optical excitation and relaxation processes. The types of questions I will address are: What are the absorption processes whereby the material gains energy from a laser pulse? How is the absorbed energy redistributed and how does the system progress to equilibrium? What happens for very large absorbed energy and what are the time scales for the various physical processes?

II. A. Interactions between Carriers and Photons

The interaction between electrons and photons is determined by the interaction Hamiltonian [9]

$$H_{\text{int}} = -\frac{e}{m_c}\mathbf{A}\cdot\mathbf{p}, \tag{40}$$

with **p** the momentum operator and **A** the single-photon vector potential operator:

$$\mathbf{A}(\mathbf{r},t) = \mathbf{A}(\mathbf{q},\omega)e^{i\mathbf{q}\cdot\mathbf{r}-\omega t}, \tag{41}$$

which is related to the electric field operator by $\mathbf{E} = -1/c\left(\partial\mathbf{A}/\partial t\right)$. The probability of an electron absorbing a photon is then given by the transition matrix element [10]

$$\begin{aligned}\left\langle \mathbf{k}'n'\left|H_{\text{int}}\right|\mathbf{k}n\right\rangle &= -\frac{e}{mc}\int\psi^{*}_{n'}(\mathbf{k}',\mathbf{r})\mathbf{A}(\mathbf{q},\omega)e^{i(\mathbf{q}\cdot\mathbf{r}-\omega t)}\cdot\mathbf{p}\psi_n(\mathbf{k},\mathbf{r})d\mathbf{r} = \\ &= -\frac{e}{mc}\mathbf{A}(\mathbf{q},\omega)\cdot\mathbf{P}_{n'n}(\mathbf{k})\,\delta_{\mathbf{k}',\mathbf{k}+\mathbf{q}}\,e^{-i\omega t}\end{aligned} \tag{42}$$

where $\psi_n(\mathbf{k},\mathbf{r})$ is the wavefunction of the electron, and we have introduced the momentum matrix element

$$\mathbf{P}_{n'n}(\mathbf{k}) = \int\psi^{*}_{n'}(\mathbf{k}',\mathbf{r})\mathbf{p}\psi_n(\mathbf{k},\mathbf{r})\,d\mathbf{r}. \tag{43}$$

The Kronecker-delta in Eq. (42) represents momentum conservation. Note, however, that because the wavelength of light is much larger than the lattice constant, $\lambda >> a$, the momentum of the photon is much smaller than that of the electron:

$$q = \frac{2\pi}{\lambda} \quad << \quad k \approx \frac{2\pi}{a} \tag{44}$$

The Kronecker-delta in Eq. (42) can therefore be replaced by $\delta_{\mathbf{k}'\mathbf{k}}$, and in an $E(k)$-plot the absorption of a photon by an electron results in a vertical transition (since the change in momentum is negligible on the scale of the reciprocal lattice vector k).

As a specific example let us consider the interaction of an electron near the top of the valence band in a direct-gap semiconductor (*i.e.*, a semiconductor for which the minimum in the conduction band and the maximum in the valence band occur at the same value of k). The photon leaves a hole behind in the valence band and creates a free electron in the conduction band, see Fig. 18. Neglecting the Coulomb interaction between the electron and the hole, the transition probability is given by [11]

$$W_{n'n} = \frac{2\pi}{\hbar}\left|\left\langle \mathbf{k}'n'\left|H_{\text{int}}\right|\mathbf{k}n\right\rangle\right|^2 \rho[\hbar\omega - (E_c - E_v)], \tag{45}$$

where n and n' denote the valence and conduction states, respectively, and ρ is the joint density of states, which is zero below the gap ($\hbar\omega < E_G = E_c - E_v$) and, for

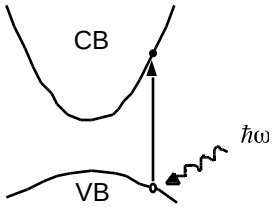

Figure 18. Vertical transition in a direct-gap semiconductor..

parabolic bands, proportional to $\sqrt{\hbar\omega - E_G}$ above the gap [11]. From Eq. (45) we thus see that the transition probability has the following dependence on frequency

$$W \quad A^2\rho \quad \frac{1}{\omega^2}\sqrt{\hbar\omega - E_G}\,. \tag{46}$$

The absorption coefficient is given by the absorbed photon energy divided by the incident energy flux ϕ, so

$$\alpha = \frac{W\hbar\omega}{\phi} \quad \frac{\sqrt{\hbar\omega - E_G}}{\omega}. \tag{47}$$

Figure 19 shows the onset of the absorption for GaAs. The deviation from the theoretical dependence of Eq. (47) shown by the dashed curve in the figure, is the so-called Urbach tail [12].

In some semiconductors the minimum in the conduction band does not coincide with the maximum in the valence band. In such indirect-gap semiconductors, transitions near the band edge require absorption or emission of a phonon or an impurity scattering event and the phonon or the impurity provides the momentum change necessary to make the indirect transition (see Fig. 20). Because indirect transitions require a three-particle interaction, they are less likely to occur than direct transitions. Figure 21 shows the absorption near the band edge for Ge. At

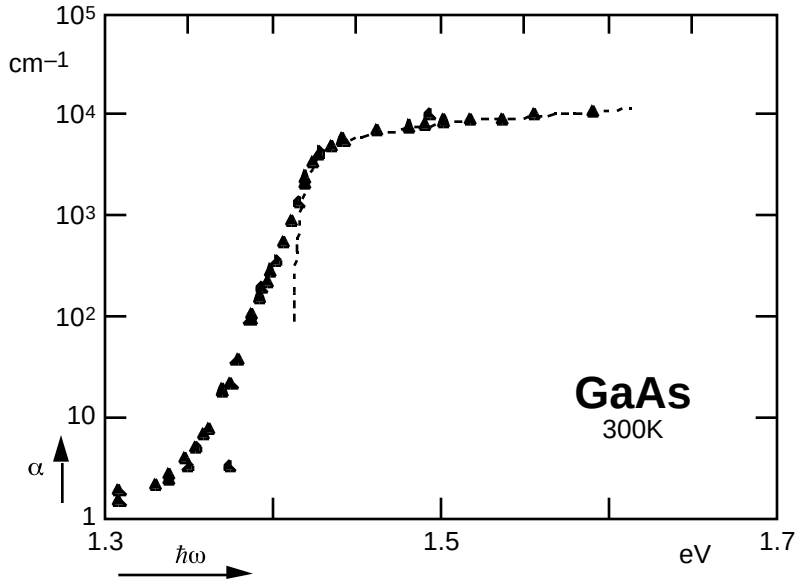

Figure 19. Onset of absorption near the bandedge for GaAs at 300 K. The dashed line represents the frequency dependence of Eq. (46). After Ref. [11].

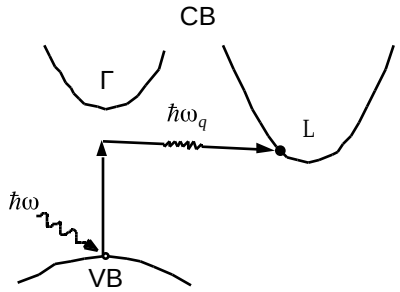

Figure 20. Optical transition in an indirect-gap semiconductor.

300 K absorption due to indirect transitions from the top of the valence band to the bottom of the L-valley at the edge of the Brillouin zone begins a little above 0.6 eV; at 0.8 eV direct transitions to the bottom of the Γ-valley (0.2 eV above the L-valley) take over.

II. B. Carrier Scattering

The excited carriers experience no 'collisions' with the periodically arranged ions — the solution to the Schrödinger equation already takes into account a periodic array of ions. They can, however, be scattered by phonons, which present a deviation from a strictly periodic arrangment, by impurities, and by other free carriers. Inelastic scattering by phonons usually dominates except at low temperature. Scattering by impurities and by other carriers are elastic processes, *i.e.*, the energy of the excited carriers remains the same.

To describe the scattering processes we introduce a (random) scattering potential $U_s(\mathbf{r},t)$. To find the scattering rate τ we need to evaluate the matrix element [10]

$$\langle \mathbf{k}'n' | U_s(\mathbf{r},t) | \mathbf{k}n \rangle = \int \psi^*_{n'}(\mathbf{k}',\mathbf{r}) U_s(\mathbf{r},t) \psi_n(\mathbf{k},\mathbf{r}) d\mathbf{r} \ . \qquad (48)$$

Let us begin by considering scattering by a charged impurity. The carriers interact

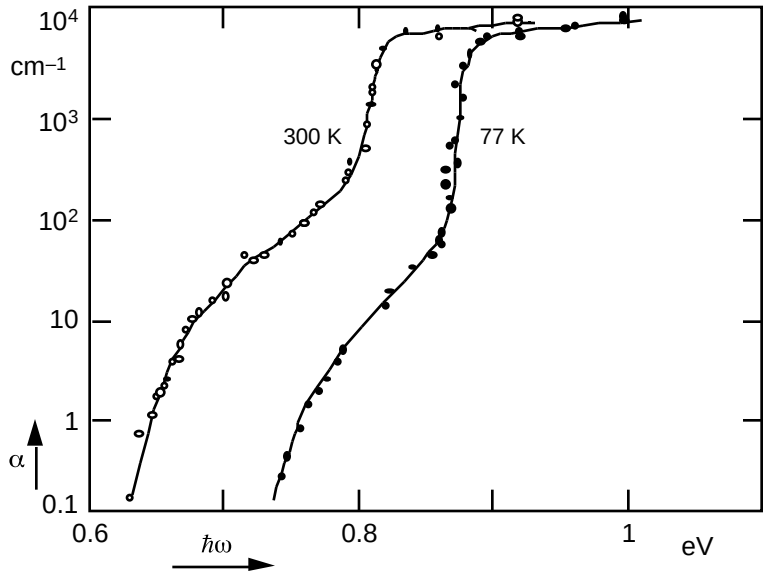

Figure 21. Onset of absorption near the bandedge for Ge at 77 and 300 K. After Ref. [11].

with charged impurities through the Coulomb potential

$$U_s(r) = \frac{q^2}{4\pi\varepsilon r}. \tag{49}$$

The scattering process is elastic, so the energy of the carrier does not change: $E(\mathbf{k}) = E(\mathbf{k}')$; the impurity merely changes the direction of the carrier ($\Delta\mathbf{k} \neq 0$). Solving the integral in Eq. (48) yields a scattering time $\tau \approx 10$ ps for a carrier energy $E = 0.5$ eV [10]. The rate scales with carrier energy as

$$\frac{1}{\tau} \quad E^{-\frac{3}{2}}. \tag{50}$$

In other words, carriers with low energy 'feel' the impurity more and are deflected over a large angle, whereas carriers with high energy undergo only slight deflection.

At high carrier density, the effect of impurity scattering is reduced by charges of opposite sign that are attracted by the impurity and screen the impurity potential. Solving the Poisson equation for a screened impurity, we find [10]

$$U_s(r) = \frac{q^2}{4\pi\varepsilon r} e^{-\frac{r}{L_D}}, \tag{51}$$

where L_D is the screening length for a nondegenerate electron gas:

$$L_D \equiv \sqrt{\frac{\varepsilon kT}{q^2 N}}, \tag{52}$$

with N the carrier density. As the carrier density goes up, the screening length becomes smaller and the scattering potential is reduced.

Scattering by phonons takes place through two different mechanisms: polar scattering and deformation potential scattering. Polar scattering occurs because phonons perturb the dipole moments between atoms. The effect is more pronounced for optical phonons (polar optical scattering) than for acoustic phonons (polar acoustic scattering or piezoelectric scattering) because optic phonons cause greater charge separation.

If a phonon causes a periodic displacement of the ions,

$$u(\mathbf{r},t) = A_q e^{i(\mathbf{q}\cdot\mathbf{r}-\omega t)}, \tag{53}$$

the dipole moments are perturbed by an amount $\delta p = q^* u$, with q^* the effective charge of the ionic cores. The field $E_{\delta p}$ of these perturbed dipoles causes a scattering potential $U_s(\mathbf{r},t) = eE_{\delta p}$ and substitution of this potential into the scattering matrix element (48) yields a scattering rate that is inversely proportional to the square of the wavevector q of the phonon [10]:

$$\frac{1}{\tau} \quad \frac{1}{q^2}. \tag{54}$$

This means that polar scattering is most pronounced for small phonon wavevectors causing the carriers to undergo only a small momentum change. Polar scattering therefore does not play a role in intervalley scattering.

In addition to perturbing the dipoles, phonons also perturb the bandgap. If the lattice constant a changes by a small amount, the bandgap will change by an amount

$$\delta E_G = D\frac{\delta a}{a}, \tag{55}$$

which is given by the deformation potential D. The change in lattice constant is related to the displacements of the ions by $\delta a \quad \partial u/\partial x$, and the scattering potential is thus given by

$$U_s(\mathbf{r},t) = D\frac{\partial u}{\partial x}. \tag{56}$$

Substituting this into the scattering matrix element (48) yields a scattering rate that is independent of phonon wavevector q. Deformation potential scattering is therefore responsible for intervalley scattering, which requires a large wavector phonon.

The final scattering process we need to consider is a binary collision between two carriers. Such a collision conserves total energy and momentum

$$\begin{aligned} \mathbf{k}_1 + \mathbf{k}_2 &= \mathbf{k}_1' + \mathbf{k}_2' \\ E(\mathbf{k}_1) + E(\mathbf{k}_2) &= E(\mathbf{k}_1') + E(\mathbf{k}_2') \end{aligned} \tag{57}$$

but randomizes both the carrier momentum and energy. The scattering rate is

$$\frac{1}{\tau} \quad f(\mathbf{k}_2)\left[1 - f(\mathbf{k}_1')\right]\left[1 - f(\mathbf{k}_2')\right], \tag{58}$$

where $f(\mathbf{k}_2)$ is the probability that initial state $\mathbf{k}_2$ is occupied and $\left[1 - f(\mathbf{k}_1')\right]$ the probability that the final state $\mathbf{k}_1'$ is empty. These probability functions can be obtained from the Boltzmann equation [3].

From Eq. (58) we see that at T = 0 K near equilibrium a carrier at the Fermi energy, $E(\mathbf{k}_1) = E_F$, cannot scatter: the collision partner must have an energy below the Fermi energy, $E(\mathbf{k}_2) < E_F$, and because of conservation of energy one (or both) of the final states must therefore be below the Fermi energy (but these states are all occupied). For carriers above the Fermi energy we find a nonzero scattering rate $\tau^{-1} \quad \left(E(\mathbf{k}_1) - E_F\right)^2$ [3], and at temperatures above zero the rate scales with the square of the temperature $\tau^{-1} \quad (kT)^2$. At T = 300 K, for instance, carrier-carrier scattering rates are on the order of 0.1 ns. Away from equilibrium, carrier-carrier scattering rates increase rapidly as the carrier density increases. Monte Carlo calculations predict a $N^{-1/3}$ dependence on carrier density [10]. Experiments show scattering times of less than 20 fs at carrier densities on the order of 10^{18} cm^{-3} (see section III.A).

II. C. Optical Excitation Processes

Figure 22 illustrates four different excitation mechanisms that occur in semiconductors. In Fig. 22*a*, a single photon creates an electron-hole pair in a direct-

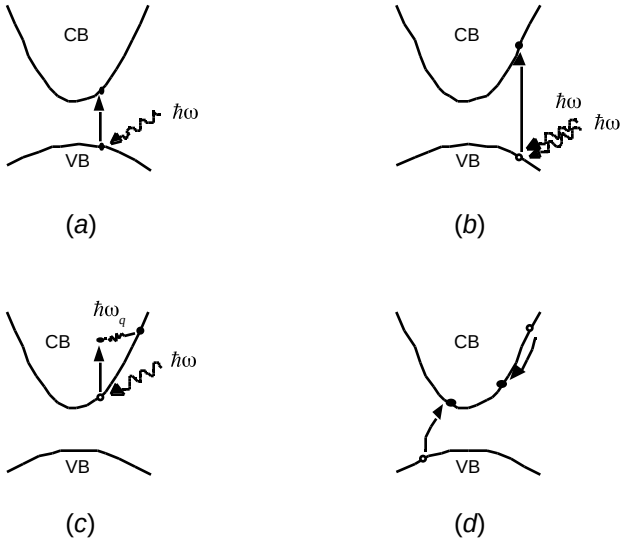

Figure 22. Excitation mechanisms in semiconductors.

gap semiconductor (in an indirect-gap semiconductor an additional phonon is required to conserve momentum). Since each photon creates a single free carrier pair, we can estimate the free-carrier density by dividing the absorbed energy by the volume into which this energy is deposited and the energy of a single photon. For a material of reflectivity R and absorption depth α^{-1}, and a laser pulse of incident fluence F, one-photon processes create a maximum carrier density

$$N \approx \frac{(1-R)F\alpha}{\hbar\omega}. \tag{59}$$

In practice the density of available states and band filling limit the carrier density that can be achieved with one-photon absorption.

Free carrier pairs can also be created through multiphoton processes. Multiphoton processes are much less likely to occur than single-photon processes, but their probability increases with increasing laser intensity. Table 2 lists the absorption depths for one-, two-, and three-photon absorption in GaAs. Figure 22*b* shows the creation of a carrier pair by two-photon absorption. This process populates different states, so it does not compete with single photon absorption and can help overcome band filling. On the other hand, it is less effective at creating carriers as two photons are required for each electron-hole pair.

Figure 22*c* shows the absorption of a photon by a carrier in the conduction band. Unless there is a resonance in the conduction band, free-electron absorption is

Type	*absorption coefficient*	α^{-1} (μm) ps pulses[(a)]	α^{-1} (μm) fs pulses[(b)]
one-photon	$\alpha_1 \approx 4 \times 10^4$ cm^{-1}	0.2	0.2
two-photon	$\alpha_2 \approx 1 \times 10^{-1}$ cm/MW	100	0.5
three-photon	$\alpha_3 \approx 3 \times 10^{-1}$ cm^3/GW^2		0.1[(c)]

Table 2. Absorption depths for GaAs. Typical values for 1-mJ, 2.0-eV laser pulses of (*a*) 10-ps and (*b*) 100-fs duration. (*c*) Estimate from bandstructure.

a three-particle process, requiring emission or absorption of a phonon or scattering off another electron. Free-carrier absorption doesn't generate new carriers, but it does increase the energy of the carriers. The interaction of free carriers with photons, given by the imaginary part of Eq. (17), has an absorption depth given by

$$\alpha = \frac{\omega_p^2}{Nc} \frac{\gamma}{\omega^2 + \gamma^2}, \tag{60}$$

where N is the free-carrier density. For a carrier density of 10^{21} cm^{-3} this yields an absorption depth $\alpha \approx 3 \times 10^2$ cm^{-1} which is relatively small compared to the absorption by carriers in the valence band.

If some of the free carriers have an excess energy above the conduction band minimum larger than the energy of the gap, impact ionization can occur (see Fig. 22*d*). The free carrier transfers some of its excess energy to an electron, creating a new electron hole pair. This process conserves the total energy of the free carriers, but increases their number.

Excitation of carriers in a semiconductor can thus be pictured as follows. Initially one-photon excitation generates electron-hole pairs. For intense laser pulses one-photon excitation will saturate due to band filling, but multiphoton excitation and free-carrier absorption will create more, and more energetic, carriers. These highly energetic carriers, in turn, can create additional carriers through impact ionization. Because of the interplay between these excitation mechanisms it is difficult to estimate the carrier density created by the laser pulse. The best one can do is to estimate an upper limit for the carrier density by replacing $\hbar\omega$ by E_G in Eq. (59). An additional difficulty is that this expression requires a value for the absorption depth which is known to vary with carrier density.

II. D. Relaxation Processes

A monochromatic laser pulse deposits free electrons in the conduction band at a number of well-defined energies. The carriers then quickly relax through a number of processes schematically illustrated in Fig. 23.

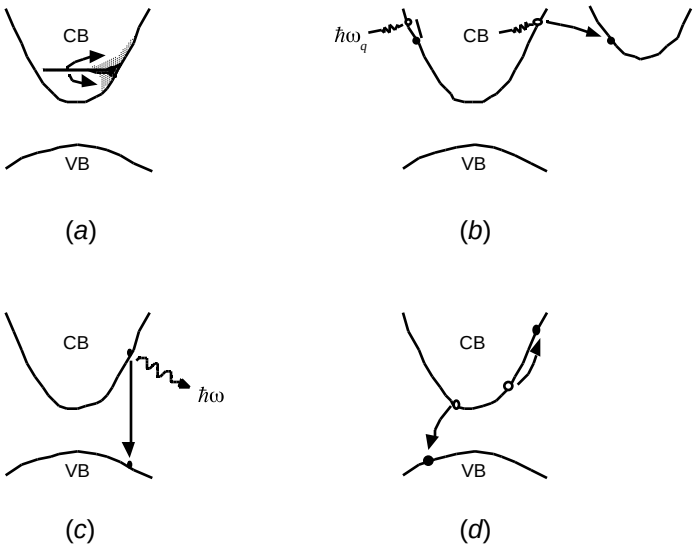

Figure 23. Relaxation processes in semiconductors.

Carrier-carrier scattering (Fig. 23*a*) causes thermalization of the nonequilibrium distribution created by the laser pulse takes place on a 10-fs time scale. This scattering process changes neither the total energy in the carriers nor the carrier density but by redistributing carriers over the band it helps overcome band filling during the excitation process.

Inelastic scattering of carriers by phonons — mostly emission of phonons by highly excited free carriers — reduces the energy of the carriers and heats the lattice (Fig. 23*b*). As we have seen in section II.B polar optical scattering is mainly responsible for small-wavevector intravalley scattering, while deformation potential scattering causes intervalley scattering. Both intravalley scattering as well as scattering from the central valley to side valleys takes place on a 100-fs time scale (see also section III.A). Scattering back from the side valleys to the central valley takes significantly longer because of the much higher density of states in the side valleys. It should be kept in mind that the energy of a typical LO phonon is generally small compared to the excess energy of the carriers. For instance, a carrier pair generated in GaAs (band gap: 1.4 eV) with a photon at 2.0 eV has 600 meV excess energy, whereas the LO phonon energy is 30 meV. Twenty phonons must therefore be emitted to rid the carrier pair of its excess energy, bringing the relaxation time due to LO phonon emission (or the lattice heating time) to approximately 2 ps.

Free electrons and holes can also recombine radiatively or nonradiatively. In a radiative recombination process, a hole and an electron of identical wavevector recombine emitting the energy difference in the form of a photon (Fig. 23*c*). This process, which lowers both the free carrier energy and the free carrier density, takes place on the 1-ns timescale. The nonradiative process shown in Fig. 23*d*, called Auger recombination, is the inverse of impact ionization: an electron and a hole recombine transferring momentum and energy to a third carrier. This three body process is proportional to N^3 and therefore important mainly at high carrier density. In fact, Auger recombination puts a cap on the carrier density, because its effect is to reduce the carrier density.

Another important mechanism that reduces the free carrier density in the region excited by the laser pulse is carrier diffusion out of the laser-excited region. If the laser spot size on the sample surface is much bigger than the absorption depth δ, then the carrier density varies only in the direction normal to the sample surface: $N(z) = N(0)e^{-z/\delta}$. In this case, the diffusion time is given by $\tau_{diffusion} = \delta^2/D_a$ [11]. The ambipolar diffusion constant D_a is related to the excited electron temperature T_e and the carrier mobility through the Einstein relation $D_a = k_B T_e \mu_a / e$ [11, 13], where k_B is the Boltzmann constant, μ_a a reduced carrier mobility for conduction electrons and valence holes, and e the magnitude of the electron charge. If the electron temperature varies in time, such as during and after femtosecond laser pulse excitation [14], the diffusion constant will also vary in time. This dependence of D_a on electronic temperature is further complicated by the implicit dependence of the carrier mobility μ_a on the electron temperature, which is not easily determined.

While an increased electron temperature resulting from femtosecond laser pulse excitation should speed up diffusion, carrier confinement slows it down [14]. This effect arises from the reduction in the bandgap in an excited semiconductor due to many-body interactions in the free carrier system [14, 15]. In laser pulse excitation, the spatial gradient of the light intensity in the material leads to a spatial gradient in the excited carrier density. The carrier-density gradient, in turn, causes a gradient in the bandgap, with a smaller bandgap coinciding with higher carrier density. Since, in the absence of diffusion, free carriers will tend towards the regions with smaller

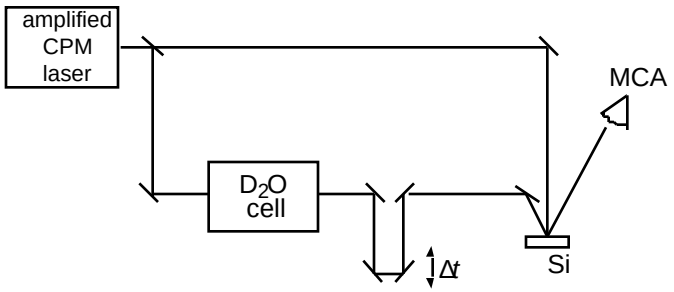

Figure 24. Schematic diagram of experimental setup to measure transient reflectivity. CPM laser = colliding pulse mode-locked laser; MCA: multi-channel analyzer. The D_2O cell serves to generate a broadband probe pulse. After Ref. [18].

bandgaps, this spatial gradient results in carrier confinement and therefore slows down diffusion [14]. Simulations and experimental measurements show that carrier-density relaxation occurs on a picosecond time scale [13, 14, 16, 17].

A number of other scattering mechanisms play a role in the distribution of the laser-deposited energy, such as scattering with plasmons (collective electronic excitations). A more detailed review of these processes can be found in Ref. [3].

III. OPTICAL MEASUREMENTS OF CARRIER AND PHONON DYNAMICS IN SOLIDS

In this section I will present a survey of relevant optical experiments on carrier and phonon dynamics in solids. Rather than being comprehensive, I will try to discuss the experiments that directly deal with the phenomena discussed in the previous section.

III. A. Carrier Dynamics

The first experiments to probe optical carrier generation in a semiconductor on the femtosecond scale were done by Shank and coworkers in 1983 [18]. Figure 24 shows a schematic diagram of the experiment. A 90-fs, 4-kJ/m^2 laser pulse of 2.0-eV photon energy strikes a Si wafer near normal incidence. The reflectivity of the central 15-μm of the 150-μm diameter excited region is probed with a broadband (1.2–2.8 eV) subpicosecond pulse. In the case of weak absorption, the reflectivity of the sample is determined by the index of refraction as follows:

$$R = \left(\frac{n-1}{n+1}\right)^2 \tag{61}$$

and from Eqs. (3) and (17) we see that for free carriers the index of refraction is given by

$$n = \sqrt{1 - \frac{\omega_p^2}{\omega^2}}\,, \tag{62}$$

with the plasma frequency given by Eq. (18): $\omega_p = \sqrt{Ne^2/(m\varepsilon_o)}$.

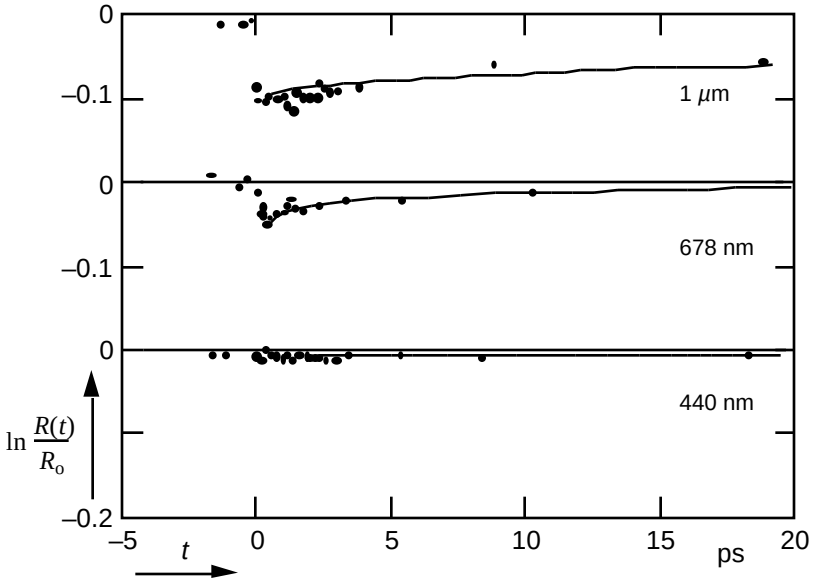

Figure 25. Changes in reflectivity at three different probe wavelengths for Si after femtosecond laser excitation. After Ref. [18].

Above a threshold incident energy of $E_{TH} \approx 1$ kJ/m^2 the sample was observed to undergo irreversible changes. Figure 25 shows the changes in reflectivity at three different wavelengths at an incident energy of 0.63 E_{TH}. The observed changes in reflectivity are attributed to changes in carrier density. As the carrier density increases, the plasma frequency goes up and, for frequencies above the plasma frequency, the index of refraction decreases. According to Eq. (61) this should in turn result in a decrease in reflectivity, which is indeed observed for $t < 1$ ps. Quantitative analysis of the reflectivity changes yields a carrier density $N \approx 5 \times 10^{21}$ cm^{-3}. The decay of the signal, caused by a decrease in carrier density in the probe region, is much slower than the measured Auger recombination rate for Si. This suggests that Auger recombination is screened at high carrier density [18].

By probing the transient absorption saturation of a 0.5-μm thin sample of GaAs,

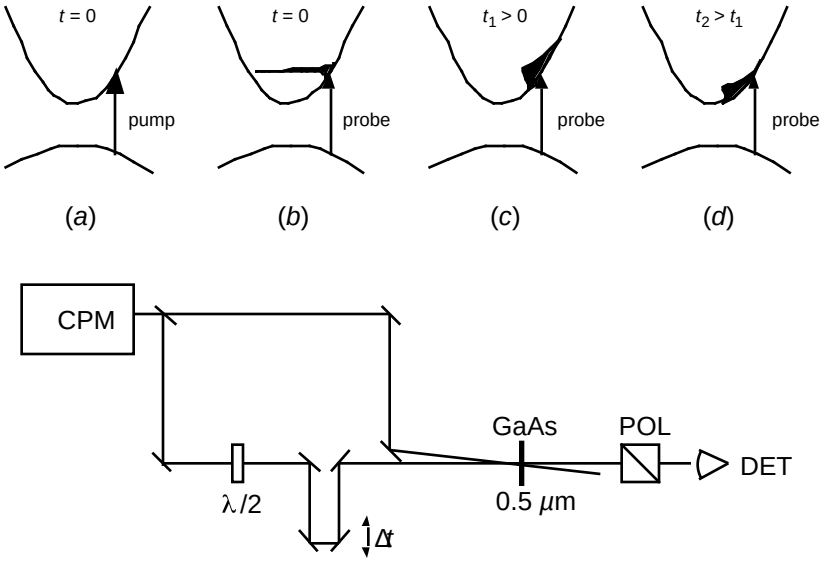

Figure 26. Schematic diagram of experimental setup to measure absorption saturation. CPM = colliding pulse mode-locked laser; λ/2 = half-wave plate; POL = polarizer; DET = detector. After Ref. [19].

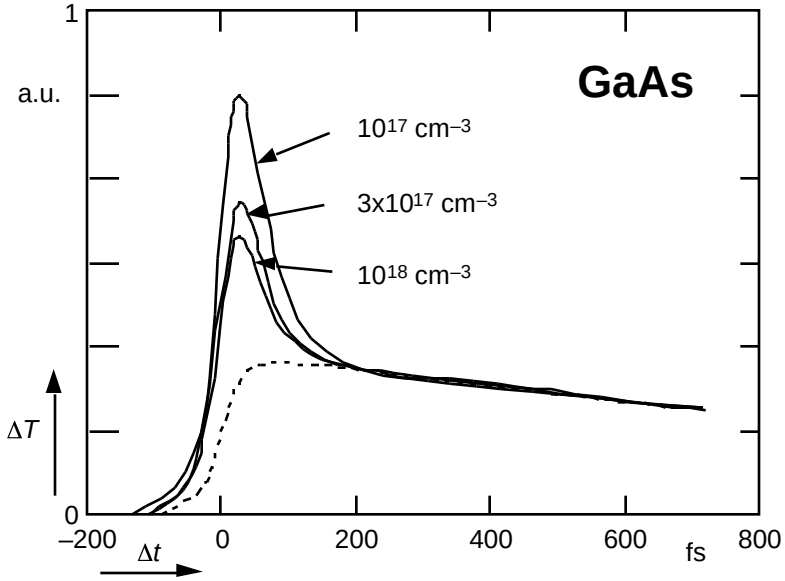

Figure 27. Change in transmittance for GaAs after femtosecond laser excitation. After Ref. [19].

Lin *et al.* were able to obtain a direct view of the dynamics of the excited carriers in the conduction band [19]. Figure 26 shows a schematic diagram of the experiment. An intense 35-fs pulse at 2 eV is used to saturate a transition from the valence band to the conduction band (Fig. 26*a*). A second pulse, equal to 20% of the pump pulse, is then used to probe the evolution of the population in the conduction band. Pump and probe have orthogonal polarizations and a detector is used to monitor the transmittance of the probe pulse through the sample. Right after excitation the population of the conduction band at the pump frequency is saturated and the probe passes through the sample registering an increased transmission on the detector (Fig. 26*b*). As the carriers thermalize the saturation diminishes and the transmission decreases (Fig. 26*c–d*). Figure 27 shows results obtained by Lin for three different carrier densities scaled so the exponential tails overlap. The dashed line shows a convolution of the laser pulse with a 1.5-ps exponential tail. The fast decay in transmittance ($\Delta t \leq 100$ fs) is due to carrier-carrier scattering, the slower 1.5-ps decay to carrier diffusion and carrier-phonon interactions. By fitting the transient saturation, the following carrier-carrier scattering times are obtained: $\tau \approx 30$ fs at $N = 10^{17}$ cm^{-3}; $\tau \approx 17$ fs at $N = 3 \times 10^{17}$ cm^{-3}; and $\tau \approx 13$ fs at $N = 10^{18}$ cm^{-3}. The scattering rate increases with increasing carrier density and, as predicted by Monte Carlo simulations [10], scales roughly as $N^{-1/3}$.

Figure 28 shows more detailed results obtained by the same group using a broadband continuum pulse (1.5-2.1 eV) as a probe [20]. Again a thin sample of GaAs is excited with a 35-fs laser pulse at 2.0 eV, creating a carrier density of about 10^{18} cm^{-3}. The pump pulse induces transitions both from the valence band and from the split-off valence band to the conduction band, putting nonequilibrium electrons at 0.5 eV and 0.2 eV above the conduction band minimum (see Fig. 28*a*). At zero delay the probe beam should therefore register absorption saturation around 2.0 and 1.7 eV (see Fig. 28*b*). The observed transient absorption spectra shown in Fig. 28*d* show a rapid onset of saturation at all photon energies, indicating that a broad distribution of carriers is created in just tens of femtoseconds. At short times ($\Delta t < 200$ fs), however, the spectra still reflect the initial population created by the pump pulse as evidenced by the two holes labeled '1' and '2,' corresponding to the transitions shown in Fig. 28*b*. As the electrons thermalize, we expect the holes in the

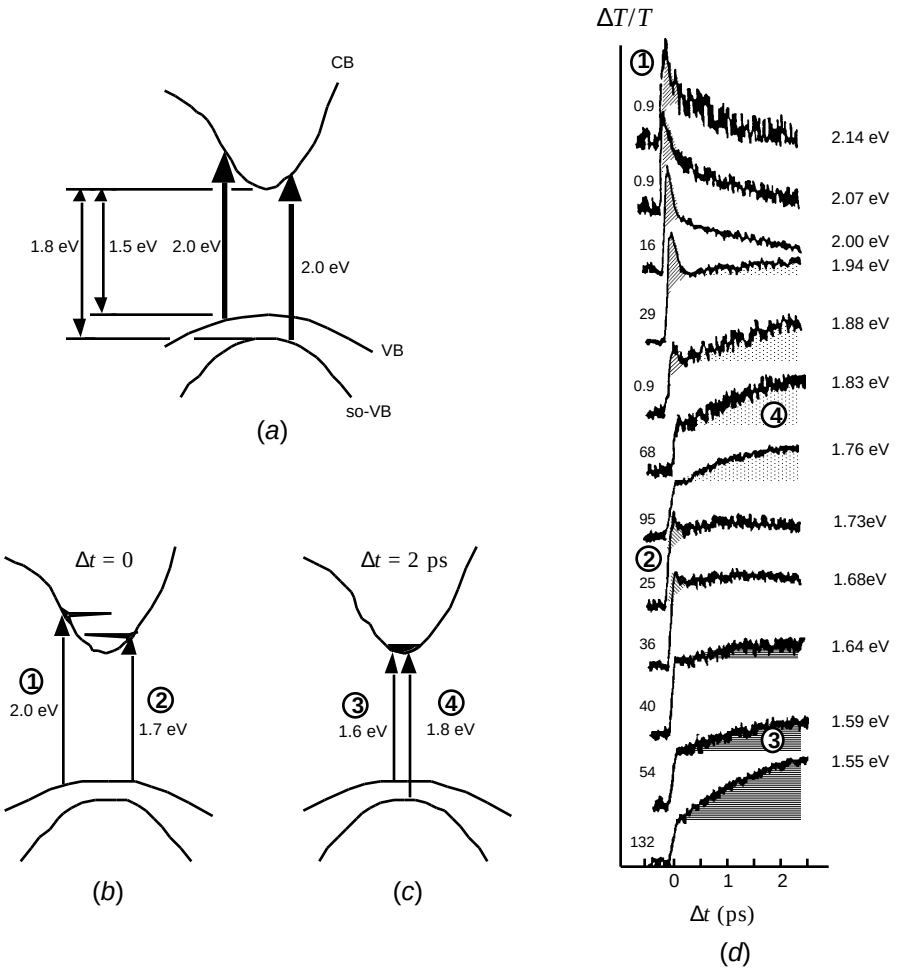

Figure 28. (*a*) Transitions induced by 2.0-eV photons in GaAs. (*b*) The populations created by the 2.0-eV photons create two spectral holes for photons at 1.7 and 2.0 eV (two additional holes for transitions from the split-off valence band lie outside the probe range). (*c*) As the electrons relax to the bottom of the conduction band, the holes shift to 1.6 and 1.8 eV. (*d*) Transient transmission of a broadband probe beam. The numbers 1–4 correspond to the transitions in (*b*) and (*c*). After Ref. [20].

absorption to disappear, which is indeed clearly visible in the spectra at 2.0 eV or higher. Finally, as the carriers accumulate at the bottom of the conduction band, the spectra show an increase in the transmission at 1.6 and 1.8 eV (see transitions labeled '3' and '4' in Figs. 28*c* and *d*).

The dynamics of the electrons observed in the spectra of Fig. 28 are due to a combination of carrier-carrier scattering and carrier relaxation (which, in turn, is due to carrier-phonon relaxation and diffusion). To separate these effects, Oudar and coworkers used a 0.5-ps laser pulse of 1.54 eV to excite electrons just 19 meV above the bandgap of GaAs [21]. Since the LO phonon energy is about 30 meV, relaxation through carrier-phonon scattering is not possible. The evolution of the transmittance of a probe pulse (1.49–1.57 eV) is shown in Fig. 29. The spectra show a hole in the transmittance at the pump frequency of 1.54 eV which disappears by about 4 ps. Modeling of the spectral hole yields a carrier-carrier relaxation time of 0.3±0.1 ps.

Carrier-phonon scattering in GaAs was studied using spontaneous Raman scattering [22]. A 0.6-ps pulse at 2.1 eV was used to create a free electron density of 2×10^{17} cm^{-3}. The free electrons relax back to the bottom of the conduction band via LO phonon emission. Using 2.1-eV photons, the excited electrons have an excess energy of about 0.6 eV, which is equivalent to the energy of 16 LO phonons. The

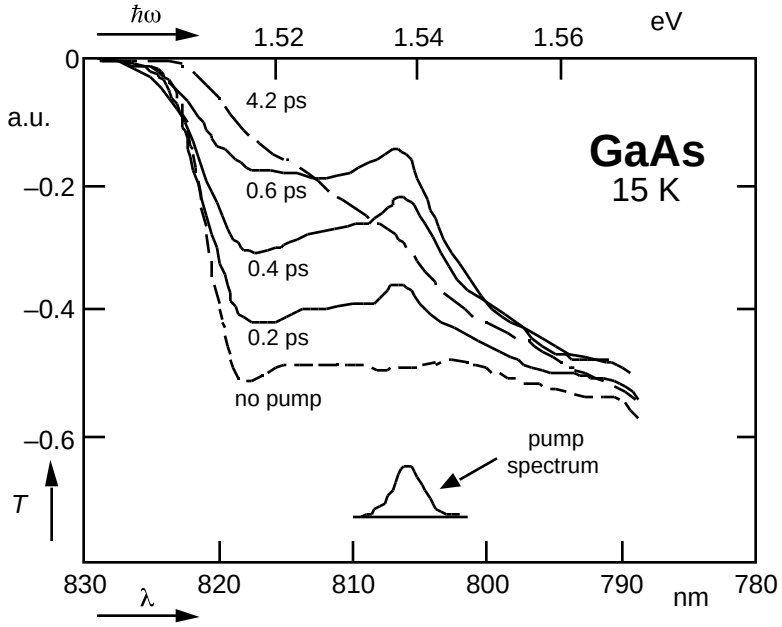

Figure 29. Transmission of a broad probe pulse for GaAs at 15 K after excitation of carriers just above the bottom of the conduction band (visible at 1.51 eV). Inset shows pump laser pulse spectrum. After Ref. [21].

phonon population was monitored by measuring the intensity of the anti-Stokes Raman signal (see Fig. 30).

Figure 31 shows that the anti-Stokes signal rises in about 2 ps and decays with a time constant of 4.0 ps at 300 K and 7.5 ps at 80 K. The rise in signal is caused by the increase in LO-phonon population that results from the LO-phonon emission of the excited carriers (see Fig. 30*c*). In the backscattering geometry used in this

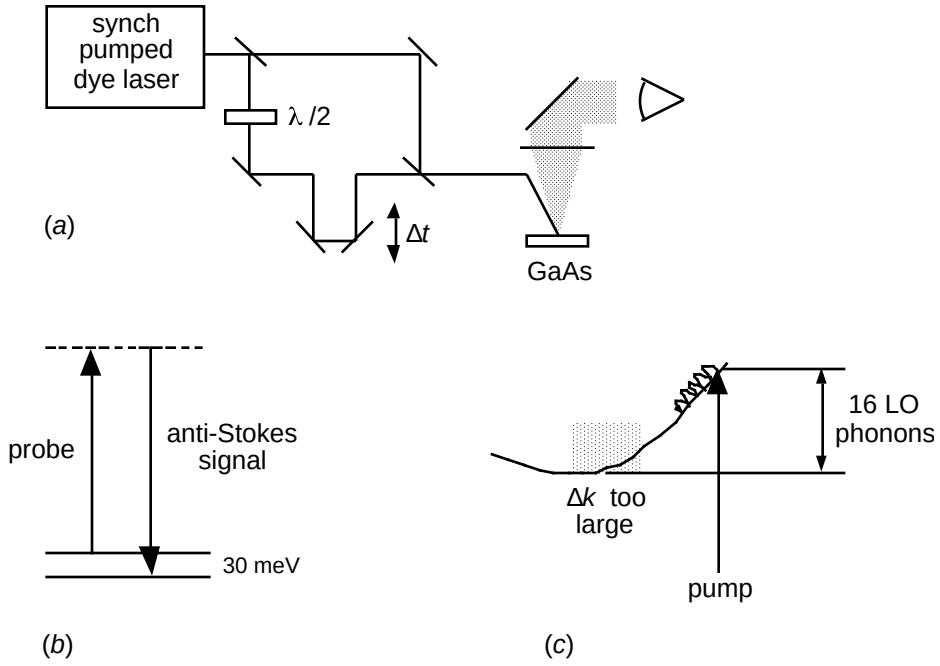

Figure 30. Measurement of the carrier-phonon scattering time after Ref. [22]. (*a*) Optical arrangement. (*b*) The probe pulse monitors the population in the LO-phonon mode. (*c*) The excited carriers relax down the side of the Γ-valley in the conductin band via a cascade of 16 LO phonons Only the first twelve of these phonons have a wavevector *q* of the right magnitude to be seen in the backscattering geometry shown in (*a*).

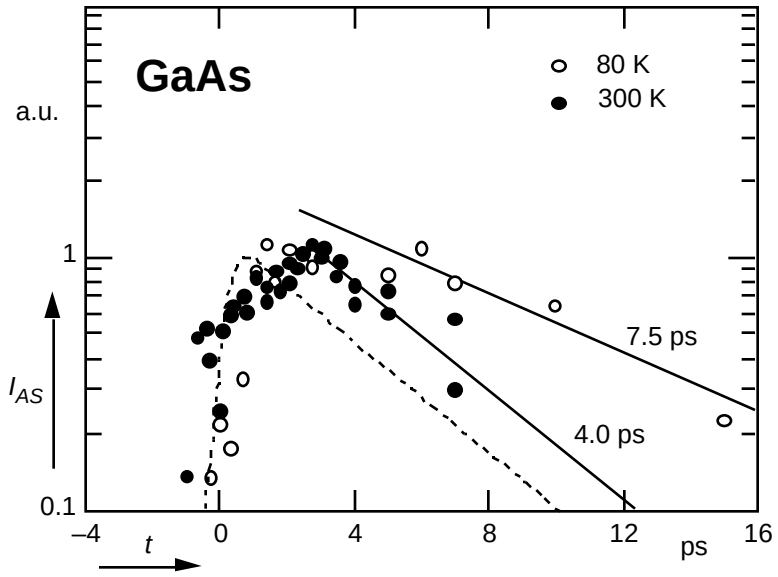

Figure 31. Evolution of spontaneous anti-Stokes Raman signal for GaAs at 80 and 300 K after subpicosecond laser excitation. After Ref. [22].

experiment, LO phonons of wavevector $q = 2k$, with k the photon wavevector, are probed; for 2.1-eV photons this corresponds to $q = 8.4 \times 10^5$ cm^{-1}. This means that only the first 12 of the 16 phonons needed for relaxation to the bottom of the conduction band are observed — the last four photons have a wavevector larger than $2k$. The 2-ps rise time therefore implies that the time for the emission of a single LO phonon takes (2 ps)/12 = 165 fs. The decay of the Raman signal reflects a decrease in the LO phonon population due to coupling of this mode to other (mainly acoustic) phonon modes. At low temperature this coupling is less effective.

Additional information on carrier-phonon dynamics was obtained using broadband absorption spectroscopy [23]. A 6-fs, 0.1-nJ broadband (1.85–2.15 eV) pump pulse was used to populate the entire bottom 600 meV of the conduction band. An indentical pulse was then used to probe the transmittance. Because of the spectral width of the pulse the transmittance is not affected by intravalley scattering — as long as the carriers remain in the Γ-valley, they cause absorption saturation. Scattering to the L and X valleys, however, reduces the population in the Γ-valley and therefore changes the transmittance (see Fig. 32). The measured transmittance is shown in Fig. 33. The data show a fast component with a 33-fs decay time due to fast scattering out of the central valley to the side valleys and a slower component due to carrier diffusion. At longer time scales (not shown) the signal increases again

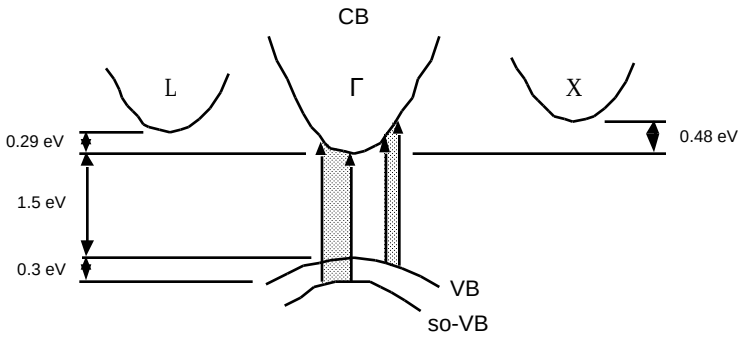

Figure 32. Region of Γ-valley of GaAs probed.by broadband (1.85–2.15 eV) pulse. The relative position of the X and L valleys is also shown.

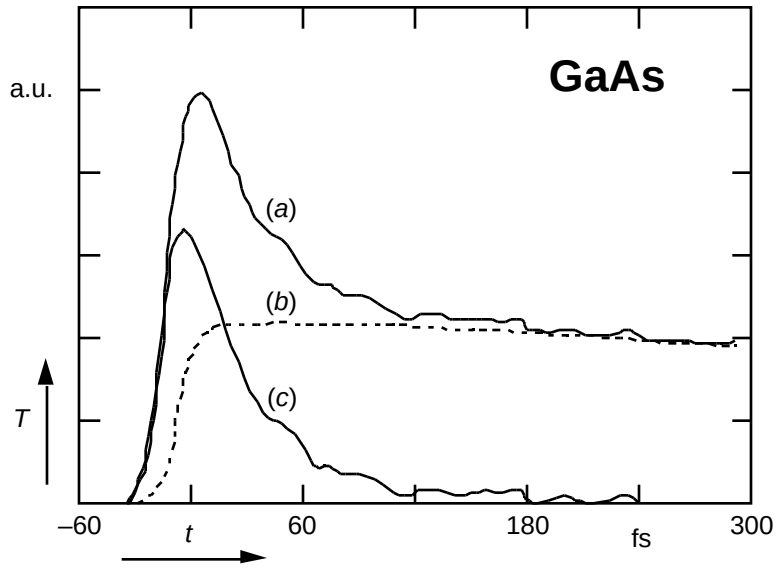

Figure 33. Transient transmittance of a broadband pulse for GaAs. (*a*) Measured signal. (*b*) Curve obtained by convoluting laser pulse envelope with a 1.5-ps exponential decay. (*c*) Transient signal obtained by subtracting (*b*) from (*a*).

due to the slower back-scattering from the side valleys to the central valleys. By cooling the sample to 35 K the bandgap increases by 0.14 eV and scattering to the X-valley is no longer possible. In this case the relaxation time of the fast component increases to about 80 fs indicating that the Γ to L intervalley scattering time is approximately 80 fs and the Γ to X scattering time about 55 fs (together these two scattering mechanisms yield the 33-fs decay time observed in Fig. 33).

III. B. Phonon Dynamics

Next we turn to the dynamics of phonons. A number of groups have studied phonon lifetimes in semiconductors using coherent anti-Stokes Raman spectroscopy [24, 25, 26]. Two picosecond laser pulses of about 2.2 eV are used to coherently drive phonons in the sample and a third laser pulse is used to monitor the decay of the coherent population created by the first two pulses. By delaying the third pulse with respect to the first two, the evolution of the coherent population can be observed. For GaAs at 77 K, the data show a 3-ps rise time (equal to the probe pulse duration) and a 7-ps decay time, indicating that the dephasing time of the coherent population is about 7-ps, close to the (6.3 ± 0.7)-ps phonon lifetime that follows from the spontaneous Raman line width [24].

An entirely different way of exciting phonons in a solid was demonstrated by Nelson and coworkers [27, 28, 29]. Using an excitation pulse shorter than the period of a phonon oscillation it is possible to impulsively excite the phonon oscillation: the laser pulse provides a sharp 'tug' that gets many phonons to oscillate in phase (see Fig. 34*a*). This method, called impulsive stimulated Raman scattering (ISRS), is illustrated in Fig. 34*b*. Two laser beams of identical frequency set up a standing wave pattern in the sample which couples to Raman active phonons. The difference in photon wavevectors **k** must match the wavevector **q** of the phonon:

$$\mathbf{k}_1 + \mathbf{k}_2 = \pm \mathbf{q} \,. \tag{63}$$

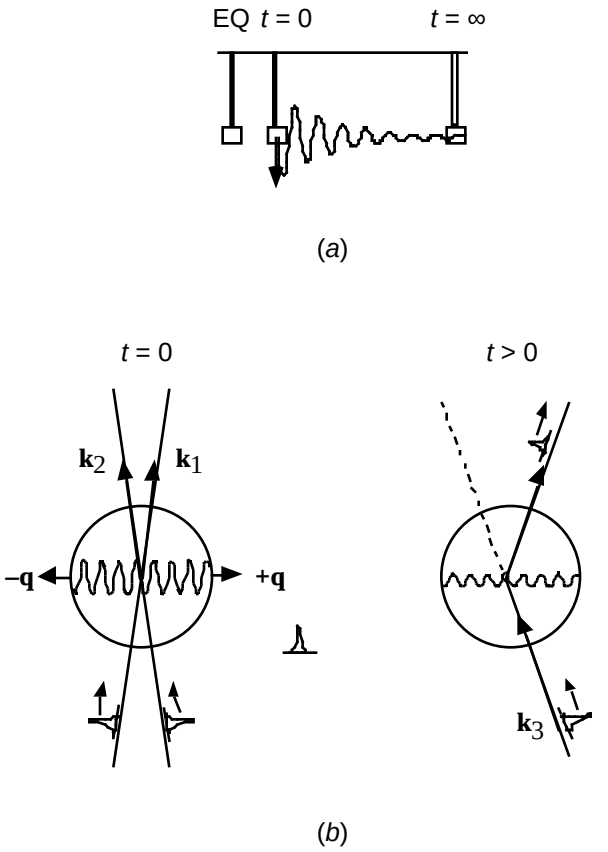

Figure 34. (*a*) Mass-on-spring model for impulsive stimulated Raman scattering (ISRS): at $t = 0$ the laser pulse provides a 'tug' which gets the atoms to oscillate coherently (*b*) Optical geometry for measuring ISRS signals. After Ref. [27].

As the phonons decay, the standing wave pattern decays. So, if a third beam strikes the decaying pattern, its scattering will reflect the amplitude of the phonon oscillation. The method is not very mode selective: since the dispersion of optic phonons is nearly flat (see Fig. 16*a*), all Raman active modes can satisfy Eq. (63). Figure 35 shows ISRS data for perylene at 18 K [27]. The beating in the signal occurs because of the beating between two Raman active modes of perylene at 80 and 104

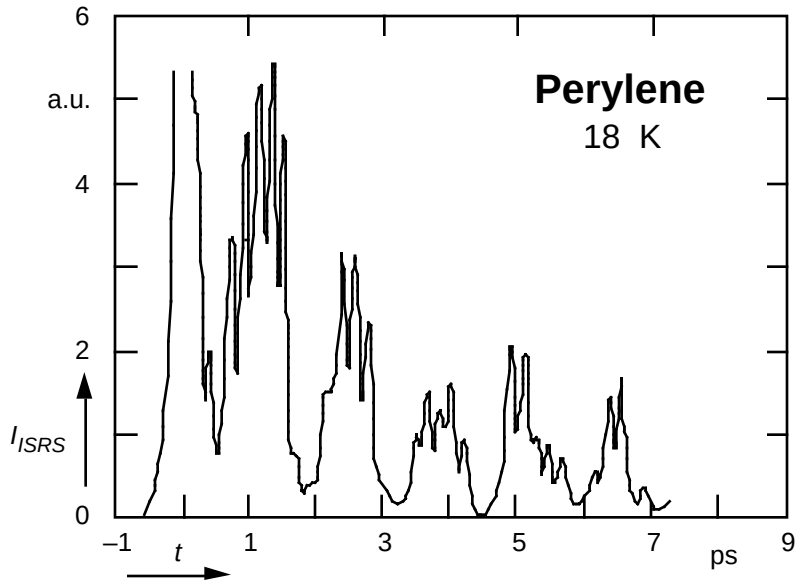

Figure 35. ISRS signal in Perylene at 18 K. After Ref. [27].

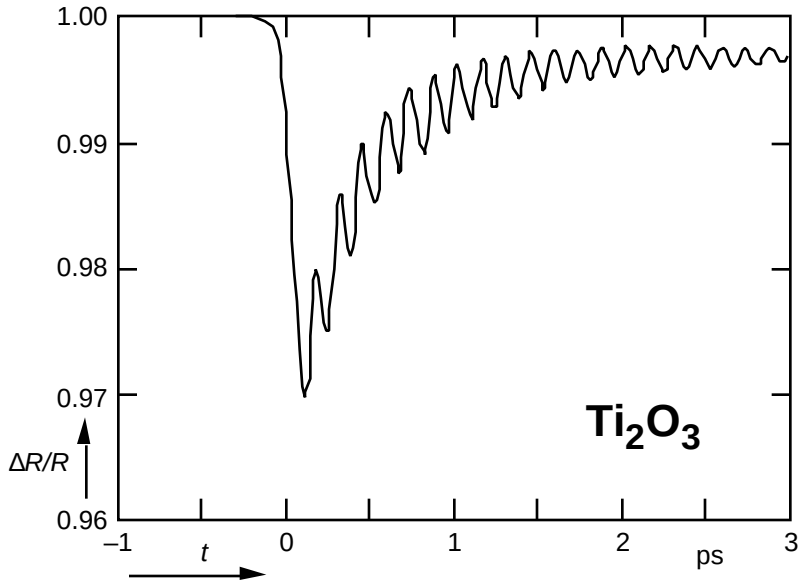

Figure 36. Transient reflectivity changes for Ti_2O_3 after excitation with a 0.1-pJ femtosecond laser pulse. After Ref. [32].

cm^{-1}. The signal decays with a time constant of about 9 ps.

In small bandgap materials a similar type of decaying phonon oscillation can also be observed in a much simpler, two-beam pump-probe geometry [30, 32]. A 60-fs, 10-pJ laser pulse at 1.98 eV is used to excite carriers in a sample and a 1-pJ pulse at the same frequency is used to measure changes in reflectivity. Figure 36 shows the large (3%) oscillations in reflectivity that occur in Ti_2O_3 following the pump pulse. In contrast to the ISRS data shown in Fig. 35, only a single-frequency oscillation at 7 THz is visible even though Ti_2O_3 has two additional Raman active modes around 9 THz. In Ti_2O_3 and other small-bandgap semiconductors and semimetals where this effect was observed, the excited mode always corresponds to a 'breathing' phonon mode (A_1 or A_{1g}). The observed oscillation is attributed to a displacive excitation of coherent phonons, as illustrated in Fig. 37*b*. Instead of coherently exciting phonons through an impulsive displacement of the ions (Fig.

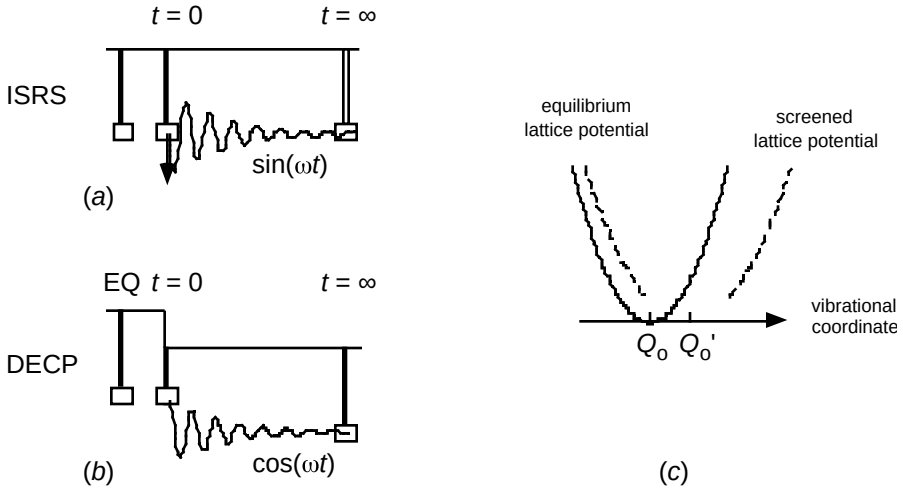

Figure 37. Mass-on-a-spring models for impulsive stimulated Raman excitation (*a*) and displacive excitation (*b*) of coherent phonons. The displacive excitation is caused by a sudden screening of the lattice potential by excited carriers. The screened potential has a different equilibrium position, displacing the ions in the lattice.

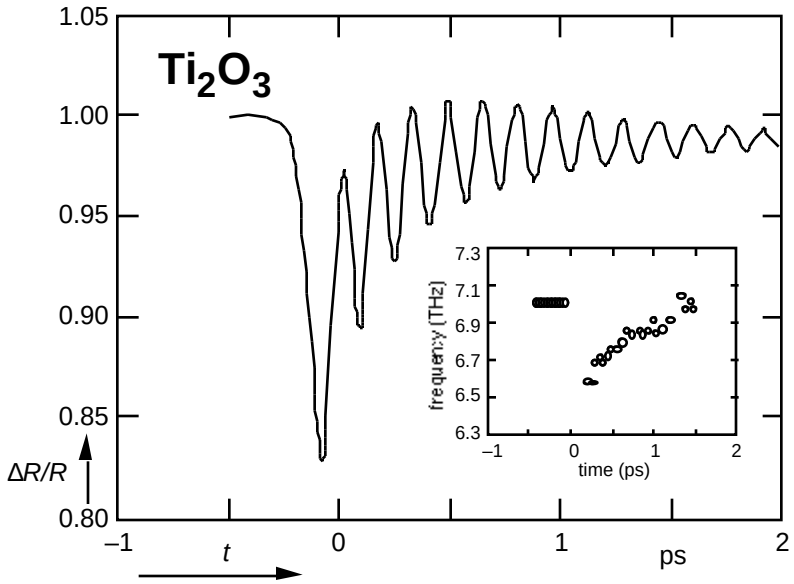

Figure 38. Transient reflectivity changes for Ti_2O_3 after excitation with a 0.1-nJ femtosecond laser pulse. Inset shows evolution of oscilllation frequency [31].

37*a*), this effect is caused by a sudden screening of the lattice potential by the photoexcited carriers (Fig. 37*c*). The screening results in a shift of the equilibrium coordinate of the ions, which in turn causes the ions to oscillate coherently (Fig. 37 *b*). Whereas impulsive stimulated Raman scattering has a sine-dependence on time, displacive excitation should have a cosine-dependence. This has indeed been verified experimentally [32].

As the pump intensity is increased, the reflectivity changes increase dramatically. Using an incident energy of 10 nJ with 2-eV, 70-fs pulses, reflectivity changes as large as 15% are observed (see Fig. 38) [31]. The inset shows the frequency of small segments of the oscillation: right after excitation the frequency of the phonon is almost 10% lower than in equilibrium, clearly showing a softening of the phonon mode (*cf.* the diminished curvature of the screened lattice potential in Fig. 37*c*).

IV. ELECTRONIC AND STRUCTURAL CHANGES INDUCED BY INTENSE SHORT LASER PULSES

As we continue to increase the pump intensity, irreversible changes occur: phonon modes soften to the point where the material loses its structure and undergoes a phase transition. In this final section I will present an overview of our recent work on laser-induced phase transitions in GaAs [33–35].

IV. A. Dielectric Properties during a Phase Transition

The field of laser-induced phase transitions in semiconductors dates back to the discovery in the 1970's that semiconductor crystals could be 'annealed' by irradiation with a short intense laser pulse [36]. Following the first experiments, two models were proposed to explain the structural change resulting from the laser excitation. One model, known as the thermal model, describes the structural change as a thermal melting process [37–39]. The thermal model assumes that the hot electrons rapidly equilibrate with the lattice by exciting lattice vibrations (through phonon

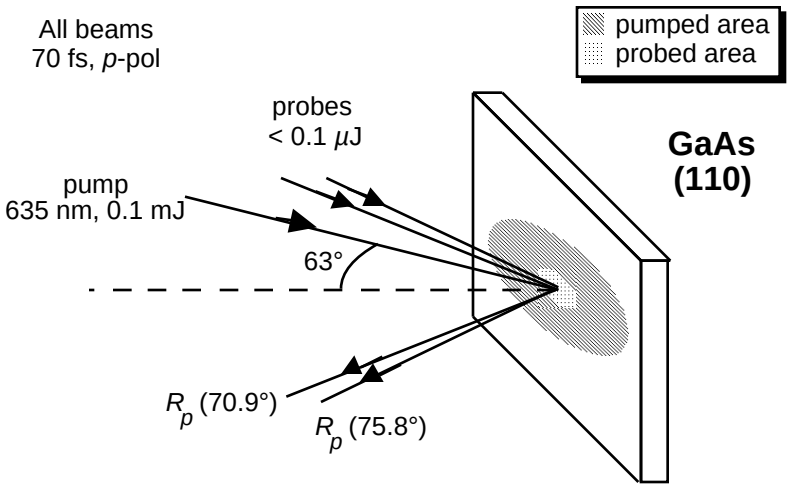

Figure 39. Two-angle probe geometry for determining the dielectric constant of GaAs. After Ref. [34].

emission). With this assumption, the laser energy deposited in the material can be treated as though it is instantly converted to heat. If the incident laser pulse is strong enough, the irradiated part of the sample will heat up to the melting temperature and undergo a transition to the liquid phase as the latent heat of fusion is supplied.

The other model, known as the plasma model, attributes the structural change to destabilization of the covalent bonds resulting directly from the electronic excitation [40, 41]. The plasma model assumes a slow rate of phonon emission by the excited electronic system compared to the energy deposition time (*i.e.*, the laser pulse width). According to this model, the structural change is driven directly by the excited electronic system. If a high enough fraction of the valence electrons is excited from bonding states to antibonding states, the crystal becomes unstable, and a structural phase transition occurs.

With nanosecond and picosecond pulses the transition from solid to liquid is thermal: because of the fast coupling between carriers and phonons, the electrons and the lattice are in thermal equilibrium and the material simply 'melts.' A detailed account of these thermal transitions, including the heating of the solid, thermal diffusion, melting, motion of the interphase boundary and recrystallization can be found in Ref. [42]. Here, I will concentrate on the highly nonequilibrium dynamics in a semiconductor excited by intense femtosecond pulses.

Reflectivity and second-harmonic generation studies of femtosecond laser-excited semiconductors show evidence of rapid changes in the material (within a few hundred femtoseconds) following the excitation [43–48]. However, interpretation of reflectivity and second-harmonic generation results is difficult because these quantities do not directly yield the behavior of intrinsic material properties. In particular, the reflectivity at a specific wavelength, polarization, and incident angle depends on both the real and imaginary parts of the dielectric constant at that wavelength. Furthermore, the measured second-harmonic radiation depends on the dielectric constant at both the fundamental and second-harmonic wavelengths as well as on the second-order susceptibility.

In the absence of a direct determination of the dielectric constant, interpretation of reflectivity and second-harmonic data requires making assumptions about the functional form of the dielectric constant, for instance that changes in the dielectric constant induced by the excitation are dominated by the free carrier contribution to the optical susceptibility [48, 18, 49]. Under this assumption, the changes in the

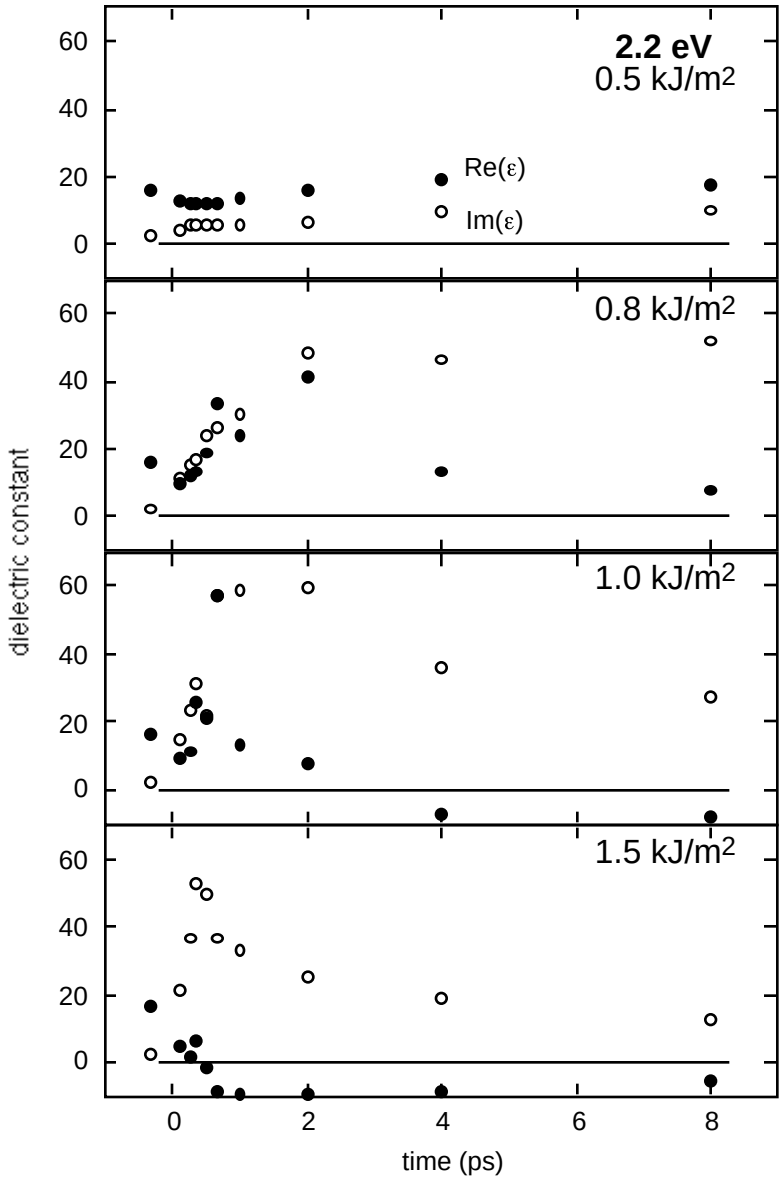

Figure 40. Dielectric constant at 2.2 eV vs. pump-probe time delay for four different pump fluences. ●: Re(ε), ○: Im (ε).

dielectric constant are described by the Drude-model formalism of section I.A (see Eq. 12). While this works well at lower excitation regimes, I will show that it leads to incorrect conclusions in the case of laser-induced disordering experiments.

We directly determined the time evolution of the real and imaginary parts of the dielectric constant using the two-angle probe technique shown in Fig. 39 [33, 34]. A 70-fs laser pulse at a photon energy of 1.9 eV is used to excite a 0.01-mm^2 area on the GaAs surface. The evolution of the reflectivity of the central 6% of the pumped area is measured at two different angles of incidence using 70-fs pulses at a photon energy of 2.2 eV. The probe beam fluence never exceeds 0.1 kJ/m^2 so as not to produce any detectable changes in the dielectric constant. To avoid cumulative damage effects, we translate the sample during data collection so that each data point is obtained at a new spot on the sample.

Each pair of reflectivity measurements is converted to a corresponding real and imaginary part of the dielectric constant by numerically inverting the Fresnel formula for reflectivity as a function of incident angle. Setting one of the probe beam angles

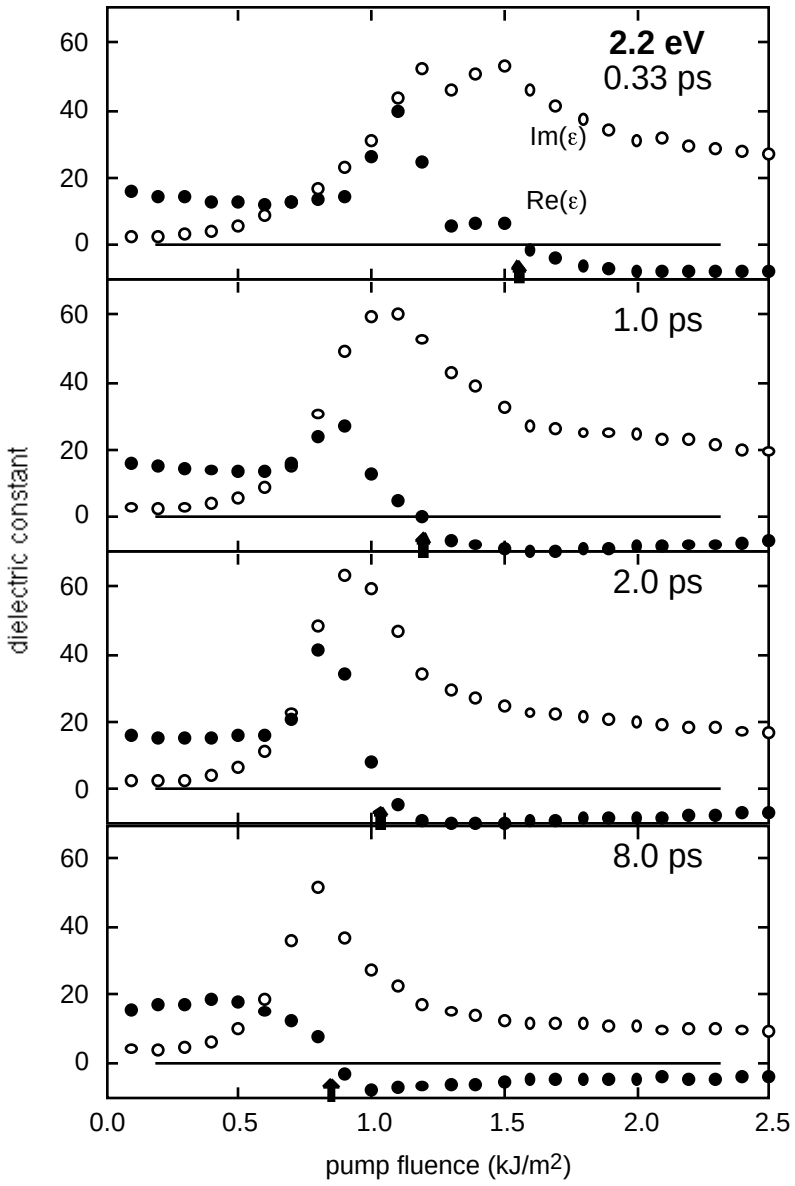

Figure 41. Dielectric constant at 2.2 eV vs. pump fluence for four different pump-probe time delays. ●: Re(ε), ○: Im (ε).

of incidence to the Brewster angle provides good sensitivity in distinguishing changes in Re(ε) from changes in Im(ε) because the *p*-polarized reflectivity at this angle is determined mainly by Im(ε) [50].

Figures 40 and 41 summarize the experimental values obtained for the dielectric function at 2.2 eV. In Fig. 40, Re(ε) (filled circles) and Im(ε) (open circles) are plotted vs. pump-probe time delay for four different excitation fluences; in Fig. 41, Re(ε) and Im(ε) are plotted vs. pump fluence at four different time delays. The change induced in the dielectric constant by the pump pulse excitation is completely different from that expected from the free carrier contribution to the optical susceptibility. In Fig. 40, at pump fluences near 1 kJ/m^2 for instance, Im(ε) starts at an initial value of about 2, rises to a peak near 60, and then drops to somewhere between 10 and 15, in strong contrast to the slight, featureless increase predicted by the Drude model. Re(ε), meanwhile, initially decreases slightly but then sharply increases before dropping through zero. Note that the zero-crossing of Re(ε) roughly coincides with the peak in Im(ε).

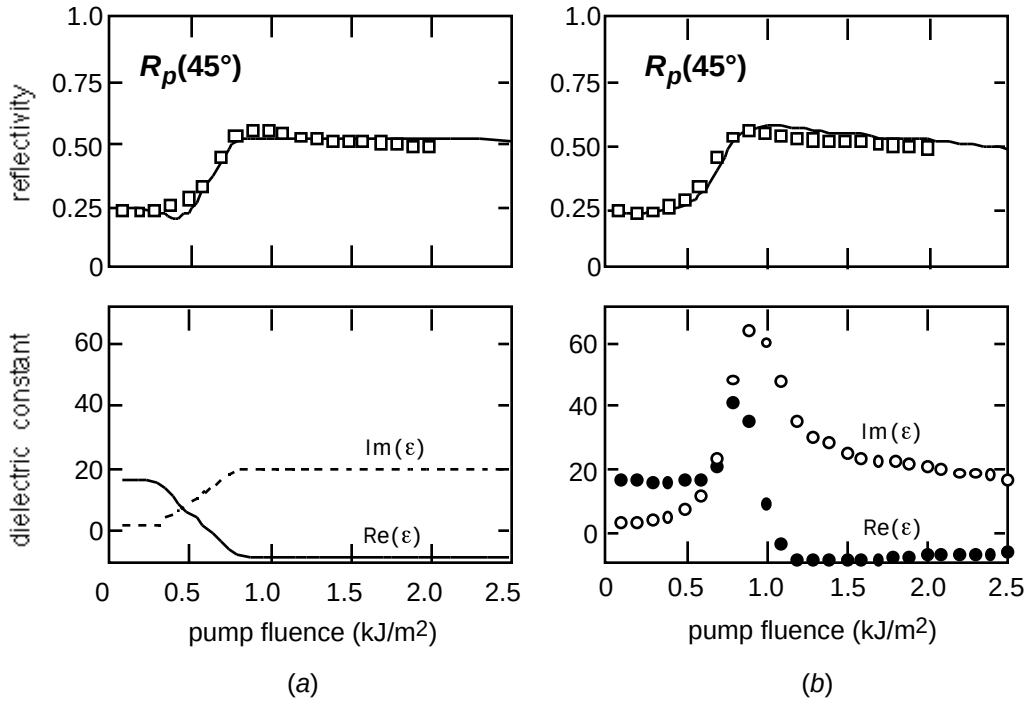

Figure 42. Comparison of (*a*) Drude-like dielectric function fitted to single-angle measurement of the reflectivity with (*b*) measured dielectric function. The top graphs show the *p*-polarized reflectivity at 45° incident angle. ———: reflectivity calculated from dielectric constant, □: measured reflectivity.

Figure 42 shows how misleading a single-angle reflectivity measurement can be. The top graph in Fig. 42*a* shows experimental values for the *p*-polarized reflectivity at a (single) incident angle of 45°, 2 ps after excitation with a 2.2-eV pump pulse. The bottom graph in Fig. 42*a* shows a Drude-like dielectric constant based on Eq. (17), adjusted to reproduce the measured 45°-reflectivity values as shown by the curve through the reflectivity data in the top graph in Fig. 42*a*. The excellent quality of the fit might lead one to conclude that the behavior of the dielectric constant is completely described by the Drude model. The measured dielectric constant, however, behaves very differently as can be seen in the bottom graph in Fig. 42*b*, which shows the experimentally determined dielectric constant at 2.2 eV plotted against pump fluence at a time delay of 2 ps (corresponding to the third graph in Fig. 41). If we use the experimentally determined dielectric constant values from this graph to calculate the corresponding *p*-polarized reflectivity at an incident angle of 45°, we obtain the curve through the data points in the top graph in Fig. 42*b* in excellent agreement with the experimental values. Note, however, how much the actual dielectric constant differs from that following from an assumed Drude-like behavior (bottom two graphs). Only the dielectric constant in Fig. 42*b* correctly accounts for the reflectivities at 45°, 70.9° and 75.8°; the Drude-like dielectric constant only correctly describes the 45° data. Notice, in particular, how the Drude assumption completely misses the strong aborption-like feature in the dielectric function which occurs at 1.0 kJ/m^2, precisely as the material undergoes a transition (see also Fig. 43).

The results shown in Figs. 40 and 41 indicate that a strong absorption peak comes into resonance with the probe frequency as a result of the excitation. The resonance behavior is most striking in Fig. 41 because the features are particularly clear when plotted versus pump fluence. This behavior must result from an interband absorption peak and not from a free carrier plasma resonance because the

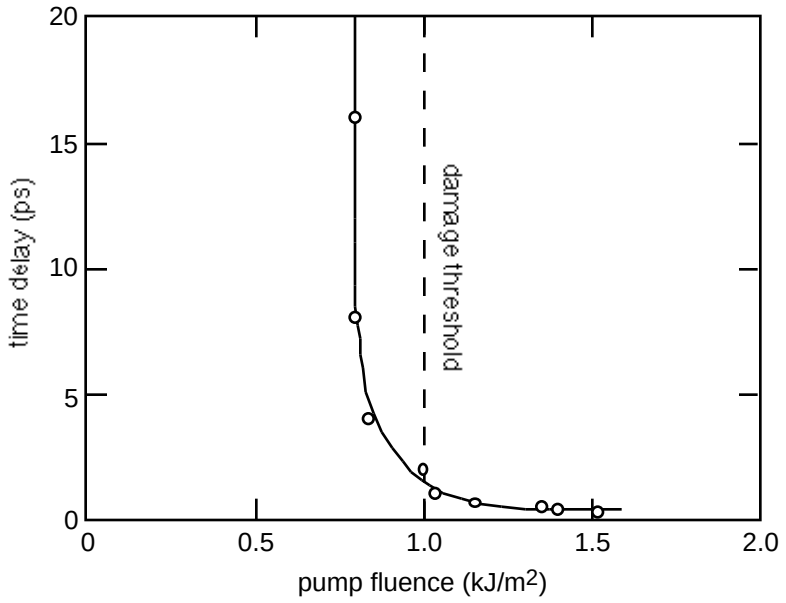

Figure 43. Pump-probe time delays at which Re(ε) = 0 for different pump fluences. The solid curve is drawn to guide the eye, and the dashed line corresponds to the damage threshold of 1.0 kJ/m^2. At fluences above this value, the induced changes in the material are irreversible while at fluences below the damage threshold, the induced changes are reversible.

zero-crossing in Re(ε) is accompanied by a peak in Im(ε) rather than by a steady increase. From the behavior of Re(ε), we can infer the time evolution of this interband absorption peak. Because Re(ε) is initially positive, the resonant frequency of the observed absorption peak evidently starts out higher than the probe frequency; it then sweeps down through the probe frequency as Re(ε) drops through zero.

The rate at which the resonant frequency of the absorption peak drops through the probe frequency depends on the strength of the excitation: the higher the pump fluence, the faster Re(ε) drops through zero. Figure 43 illustrates this dependence by showing the time delay at which Re(ε) crosses through zero plotted vs. pump fluence. For fluences around 2.0 kJ/m^2, the absorption peak comes into resonance with the probe frequency within a few hundred femtoseconds; at fluences just above 0.8 kJ/m^2, on the other hand, the absorption peak takes on the order of 10 picoseconds to come into resonance. For fluences below 0.8 kJ/m^2, Re(ε) never goes through zero, indicating that the excitation is not strong enough to bring the resonant frequency of the peak down to the probe frequency.

The dashed line in Fig. 43 at 1.0 kJ/m^2 indicates the threshold fluence for permanent damage to the sample. We determined this threshold by correlating pump pulse fluence with the size of damage spots on the sample measured through a microscope. Above the damage threshold the pump pulse induces irreversible changes in the sample while below the damage threshold the induced changes are reversible. Measurements taken several seconds after the excitation confirm that the dielectric constant eventually returns to its initial value for fluences below the damage threshold (see also Fig. 52). Note, however, that the absorption peak comes into resonance with the probe frequency even for pump fluences below this damage threshold.

Qualitatively, we can approximate the dielectric function of GaAs by a damped single harmonic oscillator with a resonant frequency equal to the average bonding-antibonding splitting [51], which in the ground state is about 4.75 eV [2, 52]. If we

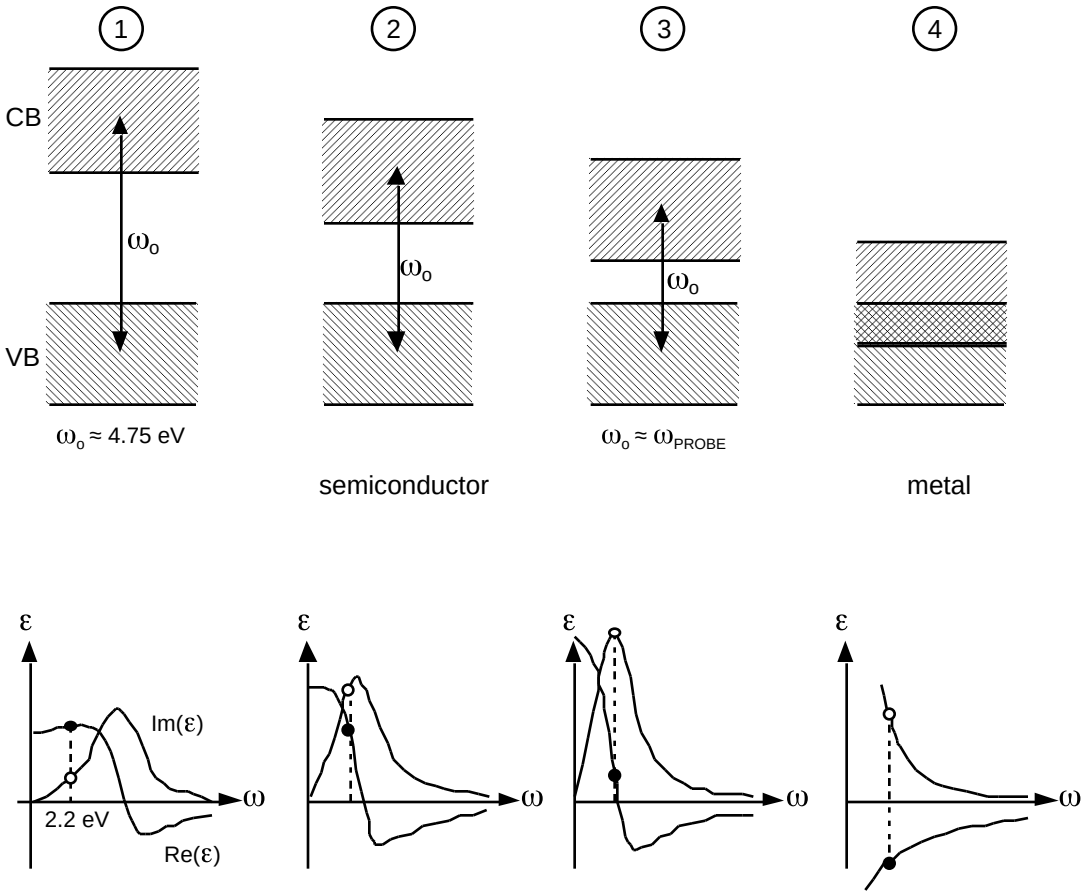

Figure 44. Schematic representation of the bandgap collapse. The pump pulse leads to a drop in the average bonding-antibonding splitting from its initial value of about 4.75 eV to below the probe photon energy of 2.2 eV. The drop in average bonding-antibonding splitting appears as a shift in the main absorption peak in the dielectric function, as illustrated at the bottom.

associate the absorption peak in the data with the harmonic oscillator peak corresponding to the bonding-antibonding splitting, then the observed sweeping of the aborption peak frequency through the probe laser frequency implies a drop in average bonding-antibonding splitting from 4.75 eV to below 2.2 eV. Note that this drop in the average splitting by more than a factor of two occurs even for fluences below the damage threshold, when the induced changes are reversible.

The laser-induced drop in the bonding-antibonding splitting is schematically illustrated in Figure 44. The average bonding-antibonding splitting $\Delta E_{b\text{-}a}$ starts out far above 2.2 eV, so the probe photon energy lies at the foot of the single-oscillator absorption peak where Im(ε) is small (step 1 in Fig. 44). After excitation, $\Delta E_{b\text{-}a}$ begins to decrease, leading to a downward shift in the resonant frequency of the single-oscillator absorption peak and therefore a rise in Im(ε) at 2.2 eV (step 2 in Fig. 44). As $\Delta E_{b\text{-}a}$ drops past 2.2 eV (step 3 in Fig. 44), Im(ε) goes through a peak. If $\Delta E_{b\text{-}a}$ drops far enough, the minimum in the conduction band will drop below the maximum in the valence band and the semiconductor will take on metallic properties (step 4 in Fig. 44).

This interpretation of the 2.2-eV data in terms of a drop in the average bonding-antibonding splitting allows us to predict qualitatively the behavior of the dielectric constant at different photon energies under similar excitation conditions. In particular, for a given excitation strength, the dielectric constant at a probe photon energy between 2.2 eV and 4.75 eV should exhibit resonance features at an earlier

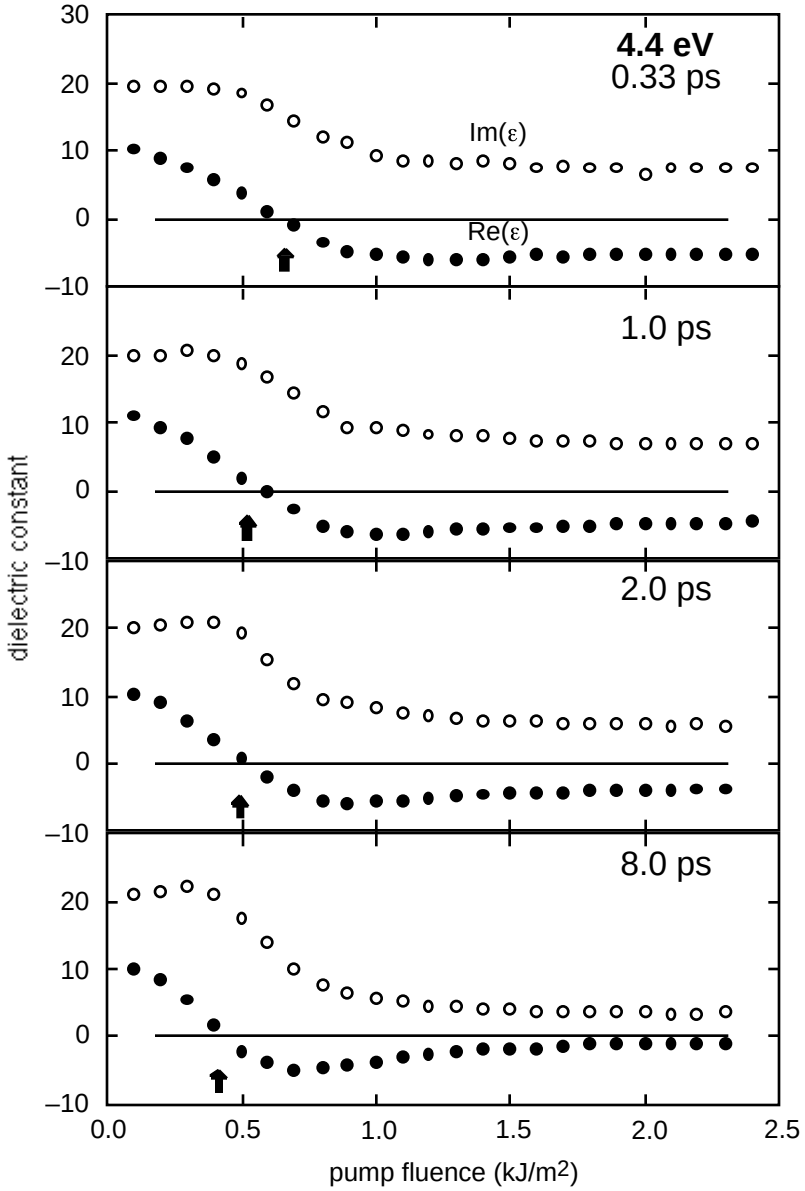

Figure 45. Dielectric constant at 4.4 eV vs. pump fluence for four different pump-probe time delays. ●: Re(ε), ○: Im (ε).

pump-probe time delay than the dielectric constant at 2.2 eV. Equivalently, for a fixed pump-probe time delay, the dielectric constant at a probe photon energy in the above range should exhibit resonance features at a lower pump fluence than the dielectric constant at 2.2 eV.

We verified this prediction by measuring the behavior of the dielectric constant using frequency-doubled probes at 4.4 eV, just below the initial value of the average bonding-antibonding splitting of GaAs. Figure 45 shows time-dependence of the 4.4-eV dielectric constant at the same four pump fluences shown in Fig. 41. Note that Im(ε) now starts near the peak and that the zero-crossing in Re(ε) occur at lower fluences than at 2.2 eV. This can also be seen in Fig. 46, which adds to Fig. 42 the corresponding points for the 4.4-eV data. At 4.4 eV, Re(ε) crosses zero for fluences as low as 0.5 kJ/m^2 well below the 0.8 kJ/m^2 required at 2.2 eV.

The behavior of the dielectric constant at 4.4 eV is indeed consistent with the proposed picture of a drop in the average bonding-antibonding splitting. Following the pump pulse excitation, $\Delta E_{b\text{-}a}$ drops from its initial value of about 4.75 eV first

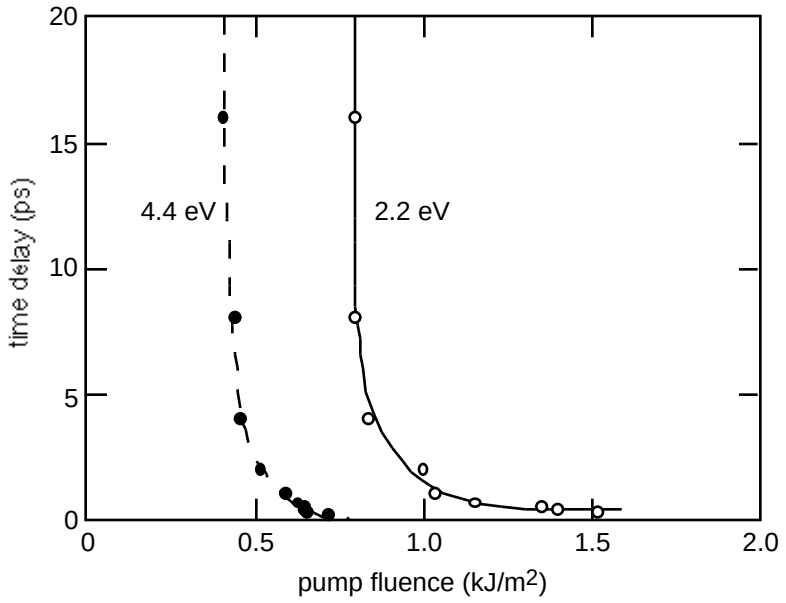

Figure 46. Pump-probe time delays at which Re(ε) = 0 for different pump fluences at both 2.2 eV and 4.4 eV. The curves are drawn to guide the eye. ●: 4.4 eV, ○: 2.2 eV.

past 4.4-eV and then continues down past 2.2-eV. A stronger excitation causes a faster drop through both probe frequencies. At pump fluences between 0.5 kJ/m^2 and 0.8 kJ/m^2, the excitation is strong enough to bring the resonant frequency of the absorption peak below 4.4 eV but not all the way down to 2.2 eV. Note that since 4.4 eV is close to the initial value of the average bonding-antibonding splitting, Im[ε(4.4 eV)] does not rise much above its initial value before coming down.

What underlying physical effects are responsible for this alteration of the band structure? To answer this question, we should examine two main sources of band structure modification: electronic screening and structural change. Through electron-hole pair generation, the pump pulse creates a large population of mobile charge carriers that can partially screen the ionic potential in the material. Since the average bonding-antibonding splitting increases with the strength of the ionic potential [2], electronic screening reduces the average bonding-antibonding splitting. A recent calculation shows that when 10% of the valence electrons are excited to the conduction band, the direct gap at the X-point in the band structure of GaAs will decrease by roughly 2 eV due to electronic screening and many-body bandgap renormalization while the direct gap at the Γ-point changes only slightly [53].

Because the strength of electronic screening increases with the free-carrier density, the effects due to screening should follow the carrier density instantaneously. Therefore, the effect of screening on the dielectric constant should be largest when the free carrier density is highest—*i.e.* immediately following the excitation. As Auger recombination and diffusion reduce the free-carrier density, the influence of electronic screening on the band structure should correspondingly decrease. However, as can be seen in Fig. 40, the changes in dielectric constant continue to grow for picoseconds following excitation, when the carrier density is already decreasing from its peak value. Clearly, electronic screening cannot, by itself, account for the observed behavior.

Since the band structure is determined by the crystal structure, changes in the atomic arrangment can also account for the observed collapse of the bandgap. Deformation of the diamond or zincblende structure in a semiconductor is known to

lead to a collapse of the band gap and a semiconductor-metal transition [2, 54–56]. Just a 10% change in average bond length is enough to cause a semiconductor-metal transition [56]. Note that an ionic velocity as small as 25 m/s is already sufficient to achieve a 10% change in the GaAs bond length within 1 ps.

In semiconductors like GaAs the covalent bonds are stabilized by the valence electrons, so excitation of a large number of electrons from bonding valence states to antibonding conduction states can lead directly to lattice instability [40, 57, 58]. If the femtosecond laser pulse is intense enough to excite this critical density of electrons, the resulting instability causes the lattice to deform — a deformation which begins immediately following the excitation but continues long after the incidence of the pump pulse. The change in the dielectric constant accompanying the lattice deformation should therefore continue to increase in the picoseconds following the excitation, in agreement with the observed behavior of the dielectric constant.

IV. B. Nonlinear Optical Properties

To further investigate the possibility of structural changes following femtosecond laser excitation, we also studied the second-order susceptibility of GaAs [35]. Because of its sensitivity to crystal symmetry, second-harmonic generation has been used by a number of researchers to study laser-induced phase transitions in semiconductors [43, 45–48, 59–61]. The sensitivity of second-harmonic generation to the symmetry properties of a nonlinear crystal arises from the dependence of second-harmonic generation on the material's second-order optical susceptibility $\chi^{(2)}$, which reflects the symmetry group of the crystal [8]. A change in the material's symmetry properties, such as may occur in a phase transition, affects $\chi^{(2)}$ and results in a change in the detected second-harmonic signal. However, the detected second-harmonic signal depends on more material properties than just $\chi^{(2)}$. In particular, it depends also on the values of the linear optical susceptibility $\chi^{(1)}$ (or, equivalently, the linear dielectric constant ε) at both the fundamental frequency ω and the second-harmonic frequency 2ω of the probe beam used for second-harmonic generation [8]. One must therefore take into account the changes in $\varepsilon(\omega)$ and $\varepsilon(2\omega)$ to extract the behavior of $\chi^{(2)}$ from second-harmonic generation measurements. As I will show, the experimentally-determined changes in linear optical properties presented in the previous section have a significant effect on the detected second-harmonic signal.

As we have seen in section I.D, the second-order susceptibility $\chi^{(2)}$ determines the nonlinear polarization $\mathbf{P}^{(2)}(2\omega)$, induced by an electric field $\mathbf{E}(\omega)$, which in turn acts as a source for the second-harmonic field $\mathbf{E}(2\omega)$, see Eqs. (32–38). The dielectric constant influences $\mathbf{P}^{(2)}(2\omega)$ by affecting the orientation and magnitude of $\mathbf{E}(\omega)$ relative to the crystallographic axes. As an example, if $\mathbf{E}(\omega)$ is oriented in the *y*-*z* plane of a crystal and at an angle θ to the *y*-axis, then the nonlinear polarization produced through the *xyz* element of the $\chi^{(2)}$ tensor, is given by

$$P_x^{(2)}(2\omega) = \chi_{xyz}^{(2)} E(\omega)\cos\theta E(\omega)\sin\theta = \tfrac{1}{2}\chi_{xyz}^{(2)} E^2(\omega)\sin(2\theta). \qquad (64)$$

Changes in the dielectric constant affect the second-order polarization through the angle of refraction θ: If the beam at frequency ω strikes the crystal at some angle θ_i, then, through Snell's Law, $\varepsilon(\omega)$ determines the angle θ inside the material that appears in Eq. (64). Thus, if the dielectric constant changes, *q* changes. In addition,

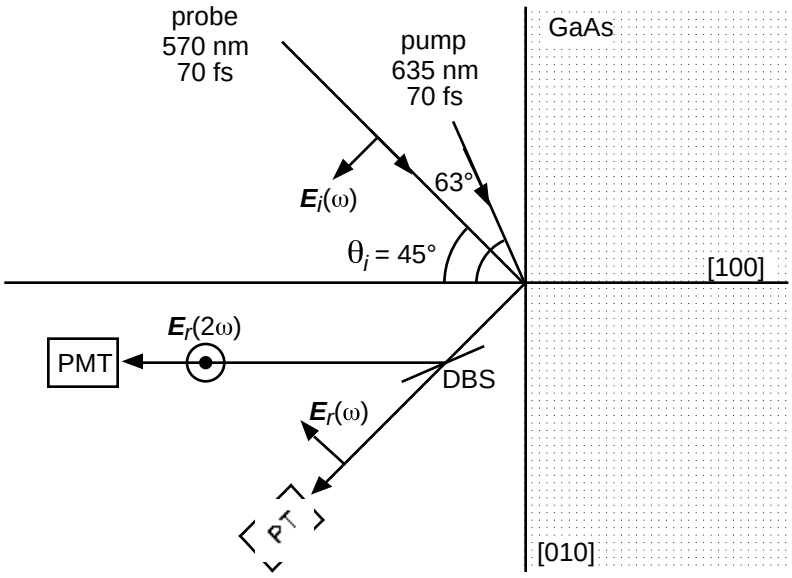

Figure 47. Probing geometry for second-harmonic generation measurements. A *p*-polarized probe beam is incident at 45° on a (100) GaAs sample in air. An ultraviolet mirror separates the reflected second-harmonic radiation, which is *s*-polarized, from the reflected fundamental radiation, which is still *p*-polarized. PMT: photomultiplier tube, PT: phototube, DBS: dichroic beamsplitter.

through the Fresnel formulas for reflection and refraction, $\varepsilon(\omega)$ also determines the magnitude of the field in the material for a given incident field. Note that the field magnitude $E(\omega)$ appearing in Eq. (64) is the field magnitude inside the material, so changes in reflectivity can have a significant effect on $\mathbf{P}^{(2)}(2\omega)$.

In addition to affecting the second-order polarization directly, the dielectric constant also affects the amount of second-harmonic radiation generated from a given $\mathbf{P}^{(2)}(2\omega)$. Firstly, the index of refraction, given by $n(\omega) = \mathrm{Re}\left[\sqrt{\varepsilon(\omega)}\right]$, determines the phase velocity for light at frequency ω. The efficiency of second-harmonic generation depends on $n(\omega) - n(2\omega)$, which determines the phase mismatch between the induced nonlinear polarization and the resulting second-harmonic field: the larger the phase mismatch, the less efficient is second-harmonic generation [8]. The phase mismatch is important especially in transmission because it determines the length scale over which second-harmonic radiation generated by the propagating fundamental (frequency ω) beam adds with the proper phase to the propagating second-harmonic beam generated earlier along the beam path. Another way in which $\varepsilon(\omega)$ and $\varepsilon(2\omega)$ affect second-harmonic generation is by determining the absorption depth at ω and at 2ω. The absorption depth can affect second-harmonic generation by limiting the interaction length over which this process takes place [8]. If the energy depleted from the fundamental beam by second-harmonic generation is negligible, as it is in our experiment, then the total amount of second-harmonic generation produced is proportional to the square of the interaction length. So if the absorption depth at one or both of the frequencies becomes smaller than the interaction length, production of second-harmonic radiation will decrease accordingly. Finally, by modifying the reflection of the second-harmonic radiation at the surface of a material, changes in $\varepsilon(2\omega)$ affect the amount of second-harmonic radiation that gets out of the material.

The second-harmonic measurements were carried out in a reflection geometry, as illustrated in Fig. 47 [35]. In this geometry, the reflected second-harmonic field amplitude is given by [7]

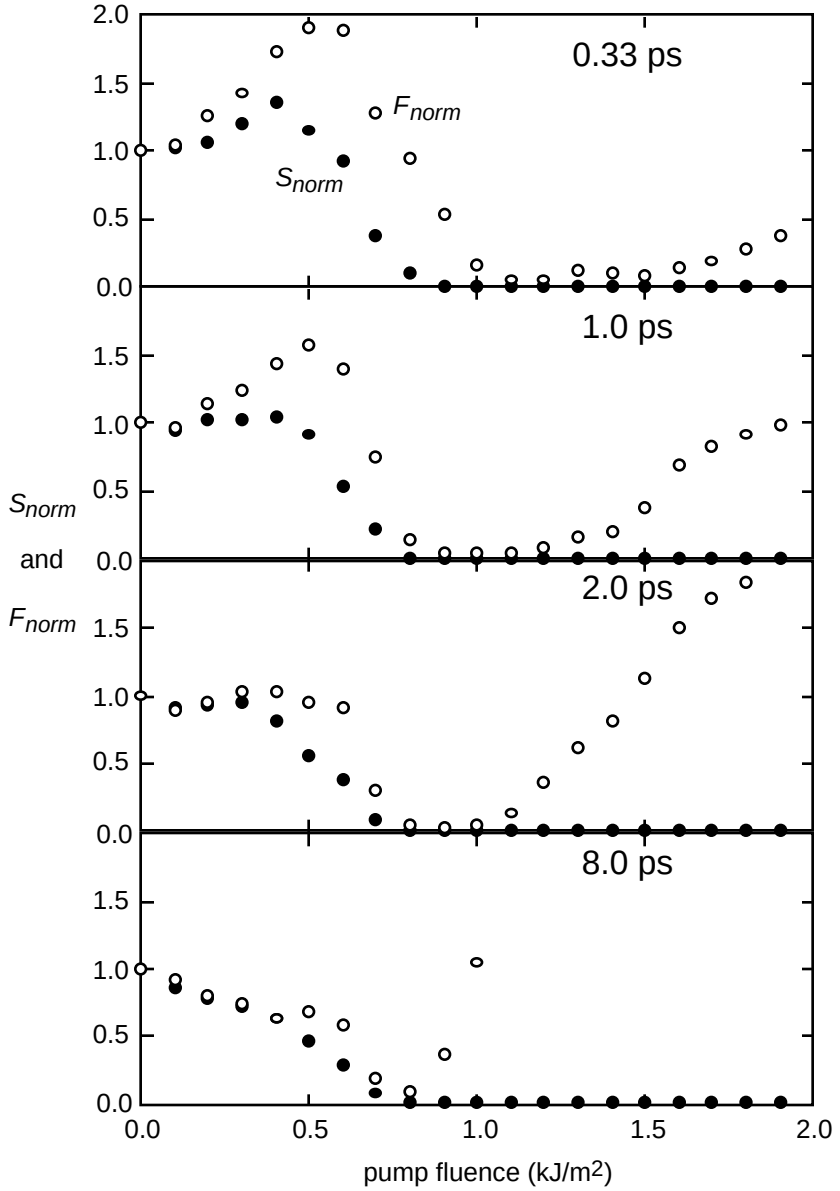

Figure 48. Normalized second-harmonic signal vs. pump fluence for four different pump-probe time delays. ●: measured second-harmonic signal, S_{norm} ; ○: second-harmonic signal calculated based solely on measured changes in dielectric constant, F_{norm} .

$$E_r(2\omega) = -4\pi P^{(2)}(2\omega)\left\{\frac{\sqrt{\varepsilon(\omega)-\sin^2\theta_i} - \sqrt{\varepsilon(2\omega)-\sin^2\theta_i}}{[\varepsilon(\omega)-\varepsilon(2\omega)]\left[\sqrt{\varepsilon(2\omega)-\sin^2\theta_i} - \cos\theta_i\right]}\right\}, \quad (65)$$

where

$$P^{(2)}(2\omega) = 2\chi^{(2)}E_i^{\,2}(\omega)\left\{\frac{4\sin\theta_i\cos^2\theta_i\sqrt{\varepsilon(\omega)-\sin^2\theta_i}}{\left[\varepsilon(\omega)\cos\theta_i + \sqrt{\varepsilon(\omega)-\sin^2\theta_i}\right]^2}\right\}. \quad (66)$$

The intensity of the reflected second-harmonic signal, and therefore the detected signal *S*, is proportional to the square of the field amplitude in Eq. (65). Note from

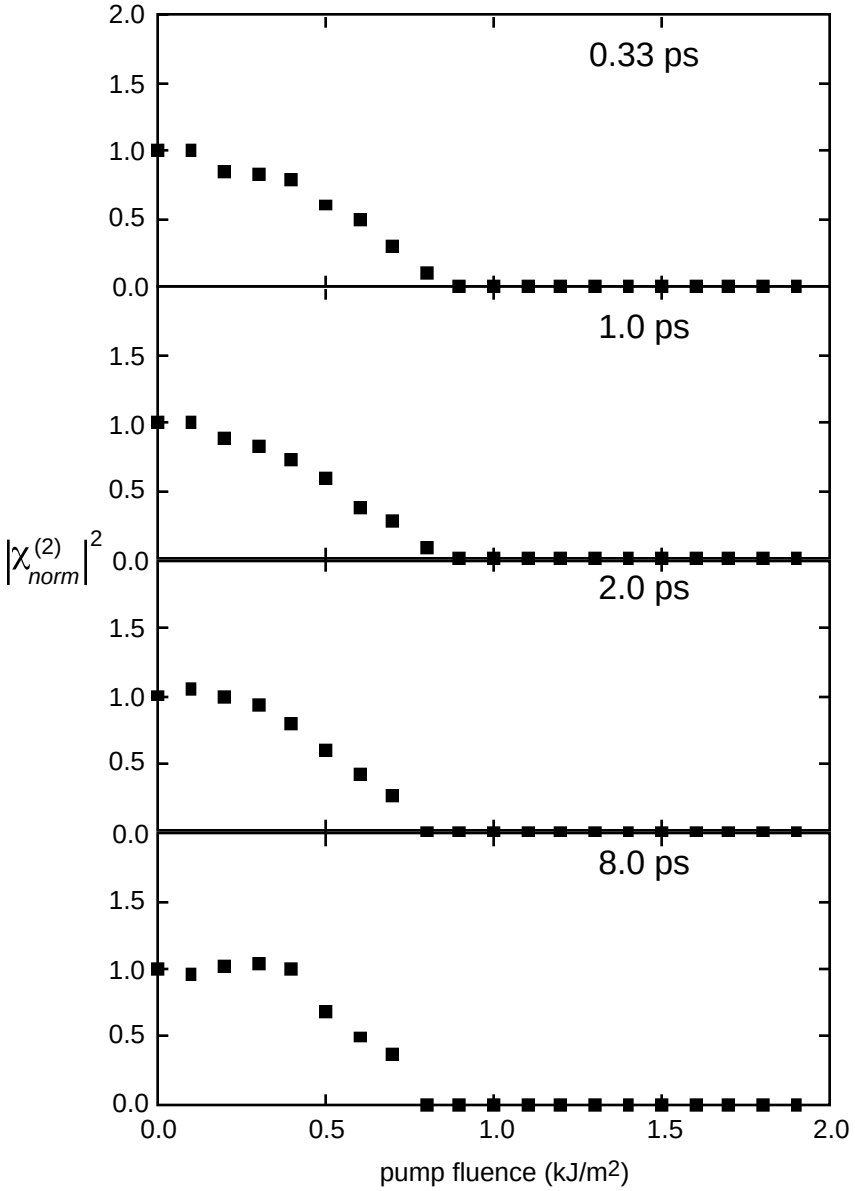

Figure 49. Square of the normalized second-order susceptibility vs. pump fluence for four different pump-probe time delays.

Eqs. (65) and (66) that we can separate the dependence of the detected signal on the dielectric constant from its dependence on the second-order susceptibility as follows:

$$\frac{S}{|E_i^2(\omega)|^2} = F[\theta_i, \varepsilon(\omega), \varepsilon(2\omega)] \times |\chi^{(2)}|^2, \quad (67)$$

where the function $F[\theta_i,\varepsilon(\omega),\varepsilon(2\omega)]$ depends only on the dielectric constant and incident angle and not on the second-order susceptibility. We can define the normalized second-harmonic signal $S_{norm}(\phi,t) \equiv S(\phi,t)/S(0,0)$, where $S(\phi,t)$ is the measured signal as a function of excitation fluence ϕ and pump-probe time delay t, and $S(0,0)$ is the second-harmonic signal detected in the absence of any excitation. Similarly, we define $F_{norm}(\phi,t) \equiv F(\phi,t)/F(0,0)$ and $\chi^{(2)}_{norm}(\phi,t) \equiv \chi^{(2)}(\phi,t) / \chi^{(2)}(0,0)$. Using the data in the previous section for $\varepsilon(\omega,\phi,t)$ and $\varepsilon(2\omega,\phi,t)$, with ω = 2.2 eV and

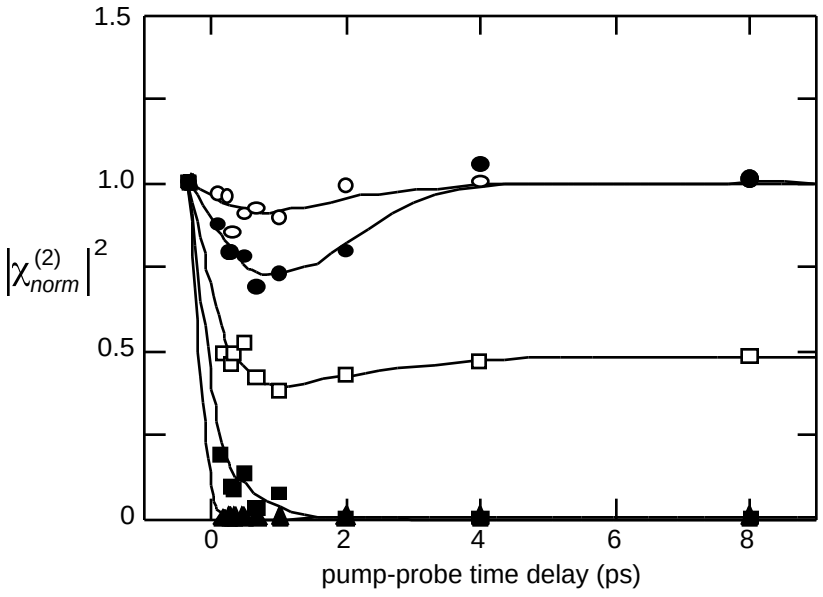

Figure 50. Square of the second-order susceptibility vs. pump-probe time delay for various pump fluences. The curves are drawn to guide the eye. ○: 0.2 kJ/m^2, ●: 0.4 kJ/m^2, □: 0.6 kJ/m^2, ■: 0.8 kJ/m^2, ▲: 1.5 kJ/m^2.

2ω = 4.4 eV, we can calculate $F_{norm}(\phi,t)$. Then, with the measured values of $S_{norm}(\phi,t)$, we get from Eq. (67) values for $\left|\chi^{(2)}_{norm}(\phi,t)\right|^2$:

$$\left|\chi^{(2)}{}_{norm}(\phi,t)\right|^2 = \frac{S_{norm}(\phi,t)}{F_{norm}(\phi,t)}. \tag{68}$$

Figure 48 summarizes the second-harmonic generation measurements and highlights the importance of taking into account the effects of changes in the linear optical susceptibility on the second-harmonic signal. The filled circles in Fig. 48 represent the measured values of the normalized second-harmonic signal $S_{norm}(\phi,t)$ plotted versus pump fluence ϕ at the same four pump-probe delays as in Figs. 41 and 45. The open circles in the figure represent the values of $F_{norm}(\phi,t)$ obtained from the measured dielectric constant at 2.2 and 4.4 eV using Eqs. (65)–(67). Note, from Eq. (68), that $F_{norm}(\phi,t)$ is identical to $S_{norm}(\phi,t)$ if $\chi^{(2)}_{norm}(\phi,t)$ is held constant at its initial value of 1. In other words, $F_{norm}(\phi,t)$ (the open circles in Fig. 48) shows the changes that result in the second-harmonic signal *solely* from the behavior of $\chi^{(1)}$ following the excitation; it does not include any effects from changes in $\chi^{(2)}$. Clearly, the changes induced in dielectric constant have a significant impact on the measured second-harmonic signal. It is important to point out, however, that while the changes in $F_{norm}(\phi,t)$ play an important role in the behavior of $S_{norm}(\phi,t)$, $F_{norm}(\phi,t)$ never drops below the experimental noise and therefore cannot account for the vanishing of $S_{norm}(\phi,t)$. Thus, $\chi^{(2)}$ must go to zero for $S_{norm}(\phi,t)$ to reach zero.

Following Eq. (5), we can now obtain $\left|\chi^{(2)}_{norm}(\phi,t)\right|^2$ by dividing $S_{norm}(\phi,t)$ (the filled circles in Fig. 48) by $F_{norm}(\phi,t)$ (the open circles in Fig. 48). The resulting values of $\left|\chi^{(2)}_{norm}(\phi)\right|^2$ appear in Fig. 48, shown at the same four pump-probe time delays as in Fig. 49. Figure 50 illustrates the corresponding time dependence of $\left|\chi^{(2)}_{norm}(t)\right|^2$. The results exhibit a range of behaviors, depending on the excitation strength. At pump fluences of 0.8 kJ/m^2 and higher, $\chi^{(2)}$ goes to zero at a rate that increases with pump fluence: at 0.8 kJ/m^2 it takes about 2 ps to reach zero while at 1.5 kJ/m^2 it

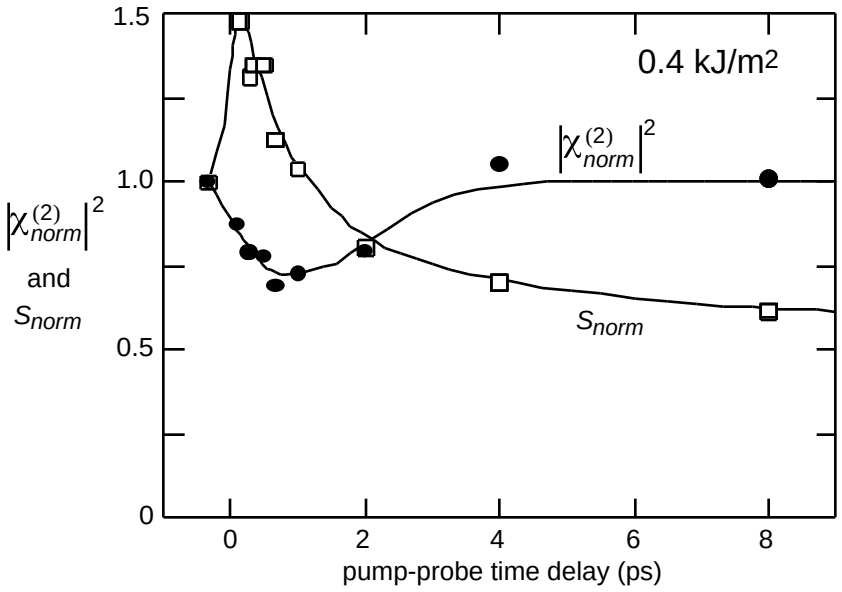

Figure 51. Normalized second-harmonic signal (□) and square of the second-order susceptibility (●) vs. pump-probe time delay at a pump fluence of 0.4 kJ/m^2. The curves are drawn to guide the eye.

reaches zero within a pump-probe time delay of 130 fs. In contrast, at pump fluences less than or equal to 0.6 kJ/m^2, $\chi^{(2)}$ undergoes a partial decrease, but it does not reach zero. For pump fluences below 0.5 kJ/m^2, $\chi^{(2)}$ recovers to its initial value on a time scale of a few picoseconds.

Figure 51 shows how important it is to take the changes in linear properties into account. At an excitation of 0.4 kJ/m^2 the second-harmonic signal first rises and then drops below its initial value within a few picoseconds. After correction for changes in the linear dielectric constant, however, we see that $|\chi^{(2)}_{norm}|^2$ first *decreases* and then *recovers* to its initial value within a few picoseconds.

We also measured both the second-harmonic signal and the linear reflectivity at

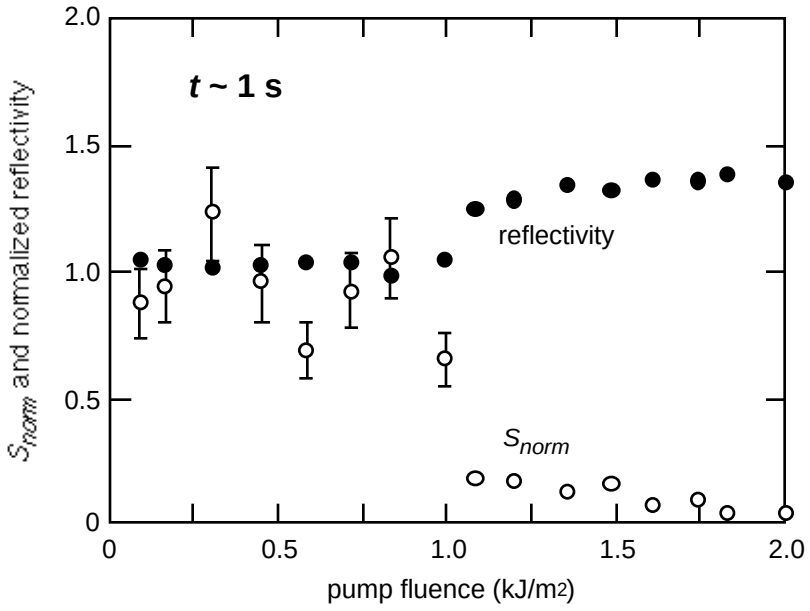

Figure 52. Normalized second-harmonic signal (○) and normalized 45° reflectivity (●) at a time delay of about a second, after the material has reached its final state.

a time delay of a few seconds (Fig. 52) as well as the second-harmonic signal at a pump-probe time delay of 100 ps (Fig. 53). Figure 52 shows a sharp demarcation at 1.0 kJ/m^2 in the final state of $\chi^{(2)}$. For excitation strengths below 1.0 kJ/m^2, both the second-harmonic signal and the linear reflectivity eventually return to their initial values. However, neither the second-harmonic signal nor the linear reflectivity ever returns to its initial value for pump fluences above 1.0 kJ/m^2. Thus, the changes induced in the material by the laser-pulse excitation are reversible if the pump fluence is below 1.0 kJ/m^2 but are irreversible if the pump fluence is above 1.0 kJ/m^2, consistent with inspection of the sample through a microscope. Figure 53 shows that for fluences greater than 0.6 kJ/m^2, once S_{norm} vanishes, it remains zero for at least 100 ps. Thus, the recovery of $\chi^{(2)}$ to its initial value at fluences between 0.6 and 1.0 kJ/m^2 occurs on a time scale which is orders of magnitude larger than the recovery times for fluences less than or equal to 0.5 kJ/m^2.

The data in Fig. 50 suggest three main regimes of behavior for $\chi^{(2)}$ following laser-pulse excitation. In the low-fluence regime, below 0.5 kJ/m^2, $\chi^{(2)}$ exhibits a partial drop but recovers to its initial value within a few picoseconds. At medium fluences, from roughly 0.8 to 1.0 kJ/m^2, $\chi^{(2)}$ drops to zero on a time scale between a few hundred femtoseconds and a few picoseconds and remains zero for over 100 ps but eventually also recovers to its initial value. In the high-fluence regime, above 1.0 kJ/m^2, $\chi^{(2)}$ drops to zero within a few hundred femtoseconds and never recovers to its initial value. While a clear boundary at 1.0 kJ/m^2 separates the medium- and high-fluence regimes, no clear boundary separates the low- and medium-fluence regimes. Rather, the behavior gradually changes from low-fluence behavior to medium-fluence behavior between 0.5 kJ/m^2 and 0.8 kJ/m^2.

At low-fluence, the behavior of $\chi^{(2)}$ is most likely dominated by electronic effects. The laser-pulse excitation of electrons from the valence to the conduction band can directly affect $\chi^{(2)}$ in a number of ways. Firstly, delocalized conduction electrons contribute little to $\chi^{(2)}$ in GaAs compared to localized valence electrons [62–64]. Thus, we expect the excitation of a high density of electrons from the valence band to the conduction band by the pump pulse ($> 10^{21}$ cm^{-3}) to cause a drop in $\chi^{(2)}$. Secondly, the excited free carriers can also reduce the interband contribution to

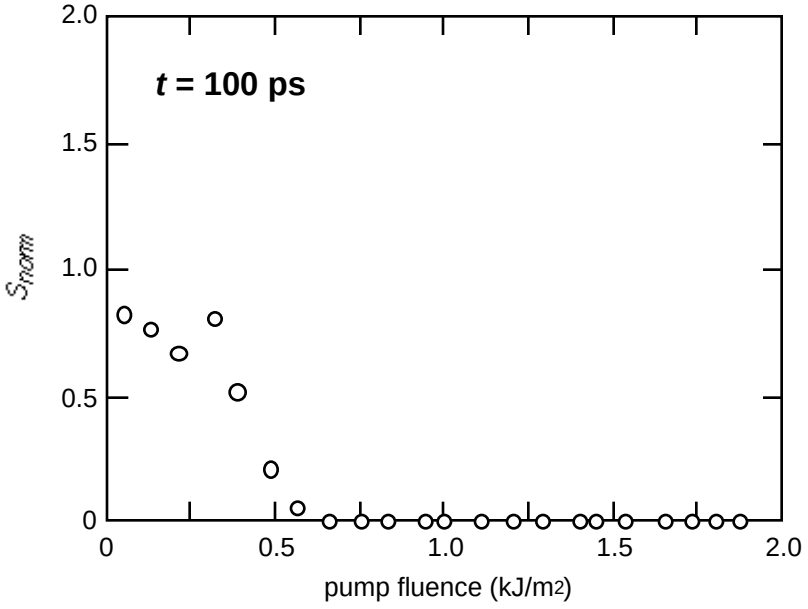

Figure 53. Normalized second-harmonic signal vs. pump fluence at a time delay of 100 ps.

$\chi^{(2)}$ by bleaching resonant transitions due to phase-space filling. In addition, electronic screening of the ionic potential by the free carriers will modify the electronic band structure [53], further affecting the interband contribution to $\chi^{(2)}$. Because the magnitude of these electronic effects should depend on the free-carrier density, we expect $\chi^{(2)}$ to return to its initial value as the excited free-carrier density relaxes through Auger recombination and diffusion following the excitation. The picosecond time scale for the observed recovery of $\chi^{(2)}$ in the low-fluence regime agrees with the time scale for Auger recombination and diffusion at free-carrier densities on the order of 10^{21} cm^{-3} [13, 14]. While the low-fluence recovery time is consistent with the expected behavior of the free carrier population, the source of the initial 1-ps delay between the excitation and the maximum change in $\chi^{(2)}$ in this fluence regime is unclear. One possible cause is that in this fluence regime the electronic excitation drives a slight structural distortion in the lattice, which is reversed when the carrier density decreases through recombination. If it is a temporary distortion of the lattice that is responsible for the partial drop in $\chi^{(2)}$, the picosecond delay in the drop would result from the timescale of the atomic motion.

At medium and high fluence, the behavior of $\chi^{(2)}$ is not consistent with electronic effects. The recovery time for $\chi^{(2)}$ exceeds 100 ps which is much larger than typical electronic relaxation times of a few picoseconds. Moreover, the vanishing of $\chi^{(2)}$ at fluences greater than 0.6 kJ/m^2 cannot be accounted for by the roughly 10% valence band depopulation achieved by the pump pulse [64]. The behavior of $\chi^{(2)}$ is therefore most likely dominated by structural changes in the lattice, which could occur on the observed time scales [58]. Recovery times for reversible structural changes should be comparable to lattice relaxation times, which are much greater than 100 ps [65].

What kind of structural change is responsible for the vanishing of second-order susceptibility? While $\chi^{(2)} = 0$ in materials that have a center of inversion [8], the vanishing of $\chi^{(2)}$ does not necessarily mean that the material has taken on a true center of inversion within each unit cell. A loss of long-range order on the scale of the wavelength of light is sufficient to cause such a drop in $\chi^{(2)}$. Experiments show that the degree of amorphization induced by low-dosage ion implantation (1×10^{12} – 6×10^{15} cm^{-2} integrated flux of 80-keV Te^+ and S^+ ions) leads to a one-to-two order of magnitude drop in $\chi^{(2)}$ [61]. The extent of ionic motion required for GaAs to lose long-range order is much smaller than that required for GaAs to take on a local center of inversion in each unit cell. Given the time scales involved in the data, a loss of long-range order is the most likely explanation for the observed drop in $\chi^{(2)}$ to zero in the medium- and high-fluence regimes.

The second-harmonic data thus support the conclusion that the pump pulse induces an instability in the covalent bonding of GaAs that leads to structural change in the lattice. The instability, which results from the excitation of a critical density of electrons from bonding valence states to antibonding conduction states [40, 57, 58] occurs instantaneously with the generation of free carriers. Because the zincblende structure is no longer stable, the ions start to move away from their equilibrium positions and the material loses its long-range order causing $\chi^{(2)}$ to vanish. A stronger excitation causes a greater instability and, therefore, faster ionic motion and a faster drop in $\chi^{(2)}$ and a faster collapse of the bandgap.

In conclusion, our experiments on GaAs show three regimes of behavior: (1) at low fluences, below 0.5 kJ/m^2, the dielectric function shows a resonance that sweeps down through 4.4 eV; the second-order susceptibility exhibits a partial drop and a recovery to its initial value within a few picoseconds, (2) at medium fluences, between 0.8 and 1.0 kJ/m^2, the dielectric function shows resonance that sweeps

down past 2.2 eV, while $\chi^{(2)}$ drops to zero but recovers to its initial value on a time scale greater than 100 ps, and (3) at high fluences, above 1.0 kJ/m^2, the changes occur more rapidly and the material undergoes permanent changes, in particular, $\chi^{(2)}$ vanishes and never recovers to its initial value.

The behavior of the dielectric function cannot be explained using a Drude model. Instead the data indicate a drop in the average bonding-antibonding splitting indicating that major changes occur in the electronic band structure of the sample. The second-harmonic data show a loss of long-range order, which suggests that structural changes occur following the laser-pulse excitation. These changes result form the destabilization of the covalent bonds and are very different from the thermal changes induced by picosecond or longer pulses.

Particularly interesting, at excitations between 0.8 and 1.0 kJ/m^2, the crystal undergoes sufficiently large structural changes to lose its long-range order but eventually reverts back to its original state. In this regime, also, the average bonding-antibonding splitting drops by more than a factor of two from 4.75 eV to beyond 2.2 eV, but it, too, recovers. The ability to induce such large transient changes in a semiconductor's structural, electronic, and optical properties may be relevant for the development of optoelectronic switching devices.

I thank Paul Callan and Li Huang for their help with the preparation of these lectures and the figures in this chapter and Prof. Claus Klingshirn and Eli Glezer for many valuable comments. The research described in section IV is sponsored by the Joint Services Electronics Program under contract number ONR N00014-89-J-1023.

REFERENCES

1. J.D. Jackson, *Classical Electrodynamics* (Wiley, New York, 1975).
2. W.A. Harrison, *Electronic Structure and the Properties of Solids: The Physics of the Chemical Bond*; (Dover, New York, 1989).
3. N.W. Ashcroft, N.D. Mermin, *Solid State Physics* (Saunders College, Philadelphia, 1976).
4. D.J. Griffiths, Introduction to Quantum Mechanics (Prentice Hall, New Jersey, 1995).
5. C. Kittel, *Introduction to Solid State Physics* (Wiley, New York, 1976).
6. R.F. Pierret, *Advanced Semiconductor Fundamentals*, Vol. VI of Modular Series on Solid State Devices (Addison Wesley, Reading, MA, 1990).
7. N. Bloembergen, and P.S. Pershan, *Phys. Rev.* **128**, 606 (1962).
8. R. Shen, *The Principles of Nonlinear Optics* (Wiley Interscience, New York, 1984).
9. E. Merzbacher, *Quantum Mechanics* (Wiley, New York , 1970).
10. M. Lundstrom, *Fundamentals of carrier transport*, Vol. X of Modular Series on Solid State Devices (Addison Wesley, Reading, MA, 1990).
11. K. Seeger, *Semiconductor Physics* (Springer Verlag, 1991).
12. C.F. Klingshirn, *Semiconductor Optics* (Springer Verlag, 1995).
13. E.J. Yoffa, *Phys. Rev. B* **21**, 2415 (1980).
14. H.M. van Driel, *Phys. Rev. B* **35**, 8166 (1987).
15. H. Kalt, M. Rinker, *Phys. Rev. B*, **45**, 1139 (1992)..
16. A. Othonos, H.M. van Driel, J.F. Young, P.J. Kelly, *Phys. Rev. B*, **43**, 6682 (1991).
17. H.R. Choo, X.F. Hu, M.C. Downer, *Appl. Phys. Lett.*, **63**, 1507 (1993).
18. C.V. Shank, R. Yen, C. Hirlimann, *Phys. Rev. Lett.* **50**, 454 (1983).
19. W.-Z. Lin, J.G. Fujimoto, E.P. Ippen, R.A. Logan, *Appl. Phys. Letts.* **50**, 124 (1987).
20. W.-Z. Lin, R.W. Schoenlein, J.G. Fujimoto, *IEEE J. of Quan. Elec.* **24**, 267 (1988).

21. J.L. Oudar, D. Hulin, A. Migus, A. Antonetti, F. Alexandre, *Phys. Rev. Lett.* **55**, 2074 (1985).
22. J.A. Kash, J.C. Tsang, J.M. Hvam, *Phys. Rev. Lett.* **54**, 2151 (1985).
23. P.C. Becker, H.L. Fragnito, C.H.B. Cruz, J. Shah, R.L. Fork, J.E. Cunningham, J.E. Henry, C.V. Shank, *Appl. Phys. Letts.* **53**, 2089 (1988).
24. D. von der Linde, J. Kuhl, H. Klingenberg, *Phys. Rev. Lett.* **44**, 1505 (1980).
25. J. Kuhl, D. von der Linde, in *Picosecond Phenomena III*, Springer Ser. Chem. Phys. **23**, 201 (1982).
26. W.E. Bron, J. Kuhl, B.K. Rhee, *Phys. Rev. B* **34**, 6961 (1986).
27. S. de Silvestri, J.G. Fujimoto, E.P. Ippen, E.B. Gamble, Jr., L.R. Williams, K.A. Nelson., *Chem. Phys. Letts.* **116**, 146 (1985).
28. L. Dhar, J.A. Rogers, K. Nelson, *Chem Rev.* **94,** 157 (1994).
29. G.P. Wiederrecht, T.P. Dougherty, L. Dhar, K.A. Nelson, D.E. Leaird, A.M. Weiner, *Phys. Rev. B* **51**, 916 (1995).
30. T.K. Cheng, S.D. Brorson, A.S. Kazeroonian, J.S. Moodera, G. Dresselhaus, M.S. Dresselhaus, E.P. Ippen, *Appl. Phys. Letts.* **57**, 1004 (1990).
31. T.K. Cheng, L.H. Acioli, J. Vidal, H.J. Zeiger, G. Dresselhaus, M.S. Dresselhaus, E.P. Ippen, *Appl. Phys. Letts.* **62**, 1901 (1993).
32. H.J. Zeiger, J. Vidal, T.K. Cheng, E.P. Ippen, G. Dresselhaus, and M.S. Dresselhaus, *Phys. Rev. B* **45**, 768 (1992).
33. Y. Siegal, E.N. Glezer, E. Mazur, *Phys. Rev. B* **49**, 16403 (1994).
34. E.N. Glezer, Y. Siegal, L. Huang, E. Mazur, *Phys. Rev. B* **51**, 6959 (1995).
35. E.N. Glezer, Y. Siegal, L. Huang, E. Mazur, *Phys. Rev. B* **51**, 9589 (1995).
36. E.I. Shtyrkov, I.B. Khaibullin, M.M. Zaripov, M.F. Galyatudinov, R.M. Bayazitov, *Sov. Phys-Semicond.,* **9**, 1309 (1976).
37. R.F. Wood, C.W. White, R.T. Young, Eds. *Semiconductors and Semimetals* Vol. **23** (Academic Press, New York, 1984).
38. A.M. Malvezzi, H. Kurz, N. Bloembergen, in *Energy Beam-Solid Interactions and Transient Thermal Processing*, Eds. D. K. Biegelsen, G.A. Rozgonyi and C.V. Shank (Materials Research Society, Pittsburgh, 1985).
39. A.M. Malvezzi, in *Excited-State Spectroscopy in Solids*, Eds. U.M. Grassano, N. Terzi (North-Holland, Amsterdam, 1987).
40. J.A. Van Vechten, R. Tsu, and F.W. Saris, *Phys. Lett.* **74A**, 422 (1979).
41. J.A.. Van Vechten, in *Semiconductors Probed by Ultrafast Laser Spectroscopy*, Ed. R.R. Alfano (Academic Press, San Diego, 1984).
42. D.K. Biegelsen, G.A. Rozgonyi, C.V. Shank, Eds., *Energy Beam-Solid Interactions and Transient Thermal Processing*, Vol. **35** (Materials Research Society, Pittsburgh, 1985).
43. C. V. Shank, R. Yen, and C. Hirlimann, *Phys. Rev. Lett.* **51**, 900 (1983)..
44. M.C. Downer, R.L. Fork, and C.V. Shank, J. Opt. Soc. Am. B **2**, 595 (1985).
45. H.W.K. Tom, G.D. Aumiller, and C.H. Brito-Cruz, *Phys. Rev. Lett.* **60**, 1438 (1988).
46. S.V. Govorkov, I.L. Shumay, W. Rudolph, and T. Schroeder, *Opt. Lett.* **16**, 1013 (1991).
47. K. Sokolowski-Tinten, H. Schulz, J. Bialkowski, and D. von der Linde, Appl Phys A **53**, 227 (1991).
48. P. N. Saeta, J. Wang, Y. Siegal, N. Bloembergen, and E. Mazur, Phys. Rev. Lett. **67**, 1023 (1991).
49. H. Kurz, and N. Bloembergen, in *Energy Beam-Solid Interactions and Transient Thermal Processing*, Eds. D.K. Biegelsen, G.A. Rozgonyi and C.V. Shank (Materials Research Society, Pittsburgh, 1985).
50. D.L. Greenaway, and G. Harbeke, *Optical Properties and Band Structure of Semiconductors*; (Pergamon Press, Oxford, 1968).
51. M.L. Cohen, and J.R. Chelikowsky, *Electronic Structure and Optical Properties of Semiconductors*; (Springer-Verlag, Berlin, 1988).

52. D.E. Aspnes, G.P. Schwartz, G.J. Gualtieri, A.A. Studna, and B. Schwartz, *J. Electrochem. Soc.* **128**, 590 (1981).
53. D.H. Kim, H. Ehrenreich, and E. Runge, Solid State Commun. **89**, 119 (1994).
54. V.M. Glazov, S.N. Chizhevskaya, and N.N. Glagoleva, *Liquid Semiconductors*; (Plenum Press, New York, 1969).
55. W. Jank, and J. Hafner, *J. Non-Crystalline Solids* **114**, 16 (1989).
56. S. Froyen, and M. L. Cohen, Phys. Rev. B **28**, 3258 (1983).
57. R. Biswas, and V. Ambegoakar, *Phys. Rev. B* **26**, 1980 (1982).
58. P. Stampfli, and K.H. Bennemann, *Phys. Rev. B* **42**, 7163 (1990).
59. T. Schröder, W. Rudolph, S.V. Govorkov, and I.L. Shumai, Appl. Phys. A **51**, 1438 (1990).
60. J.-M. Liu, A. M. Malvezzi, and N. Bloembergen, in *Energy Beam-Solid Interactions and Transient Thermal Processing*, Eds. D. K. Biegelsen, G.A. Rozgonyi and C.V. Shank (Materials Research Society, Pittsburgh, 1985).
61. S.A. Akhmanov, V.I. Emel'yanov, N.I. Koroteev, and V.N. Seminogov, *Sov Phys Usp.* **28**, 1084 (1985).
62. N. Bloembergen, R.K. Chang, S.S. Jha, and C.H. Lee, *Phys. Rev.* **174**, 813 (1968).
63. S.A. Akhmanov, N.I. Koroteev, G.A. Paitan, I.L. Shumay, M.V. Galjautdinov, I.B. Khaibullin, and E.I. Shtyrkov, *Opt. Comm.* **47**, 202 (1983).
64. S.A. Akhmanov, M.F. Galyautdinov, N.I. Koroteev, G.A. Paityan, I.B. Khaibullin, E.I. Shtyrkov, and I.L. Shumai, *Bull. Acad. Sci. USSR, Phys. Ser.* **49**, 86 (1985).
65. F. Spaepen, in *Ultrafast Phenomena V*, Eds. G.R. Fleming and A.E. Siegman (Springer-Verlag, Berlin, 1986).